Numerical Model of the Time-Dependent Water-Time Circulation of the New York Bight

Y. Hsueh, K.C. Chen, and G.O. Marmorino
Department of Oceanography
Florida State University

Prepared under Contract from National Oceanic and Atmospheric Administration

December 1982

A Numerical Model of the Time-Dependent Winter-Time Circulation of the New York Bight

Y. Hsueh, K.C. Chen, and G.O. Marmorino
Department of Oceanography
Florida State University

Prepared under contract from
National Oceanic and Atmospheric Administration

December 1982

Foreward

This report gives a comprehensive account of an effort to develop a numerical model of the barotropic response of the New York Bight to surface winds and to impinging disturbances across the Long Island shelf. The model permits predictions to be made of sub-inertial period sea-level fluctuations and transports in the Bight. The capability of being able to predict these physical parameters aids in the management of the coastal water resources in general and facilitates future efforts that may involve long-term monitoring of the coastal environment.

1. Introduction

The New York Bight is generally defined as the part of the U.S. continental shelf that extends from Montauk Point, New York to Cape May, New Jersey. Earlier works on the Bight were primarily descriptive until about 1973 when a series of direct current measurements began as a part of the Marine Ecosystems Analysis (MESA) Program under the auspices of the National Oceanic and Atmospheric Administration. (See Beardsley and Boicourt (1981) for a review of research results derived from works done before the MESA data become generally available.) Analyses of long-term continuous current-meter data from MESA have pointed clearly to surface winds, particularly winter-time storms, as the most important source for time-dependent current fluctuations in the Bight (Mayer, Hansen, and Ortman, 1979). Storm winds to the southeast during the winter are also effective in generating longitudinal flows in the Hudson Shelf Valley. The sharp change in the coastline orientation at the head of the Valley and bottom friction all tend to channel the flow along the valley axis, as is evident in an earlier steady-state model study of the bottom pressure distribution during a three-day winter-storm episode (Hsueh, 1980). The steady-state result is necessarily an approximation in which a time-varying response is represented by the average. How good is this approximation? To what extent the responses to individual storms that pass in succession are independent from one another? To gain an understanding of these and other issues that pertain to the transient response of the flow both on the continental shelf and in the Valley, a study of the time-dependent circulation in the New York Bight is undertaken. This report outlines the development

of a numerical model of the winter-time circulation in the New York Bight that is driven by the wind and by an upstream flow across the Long Island shelf. The model domain is comprised of the shelf area bounded offshore by the 100-fathom isobath and inshore by the coastline from Wildwood, New Jersey to Shinnecock Inlet, New York. (See Fig. 1 for the geographic setting of the model area). Observed winds at the John F. Kennedy airport are used with a bulk aerodynamic formula for the derivation of a wind-stress field that is applied uniformly over the entire model domain. Longshore (northeast-southwest) components of flow observed at current meter mooring stations P31 and P32 provide a basis from which a cross-shelf (northwest-southeast) bottom pressure distribution is derived as an up-stream condition. The model is run from 7 March to 30 April 1975, a common period for which direct current measurements are available at all of the mooring sites in Fig. 1.

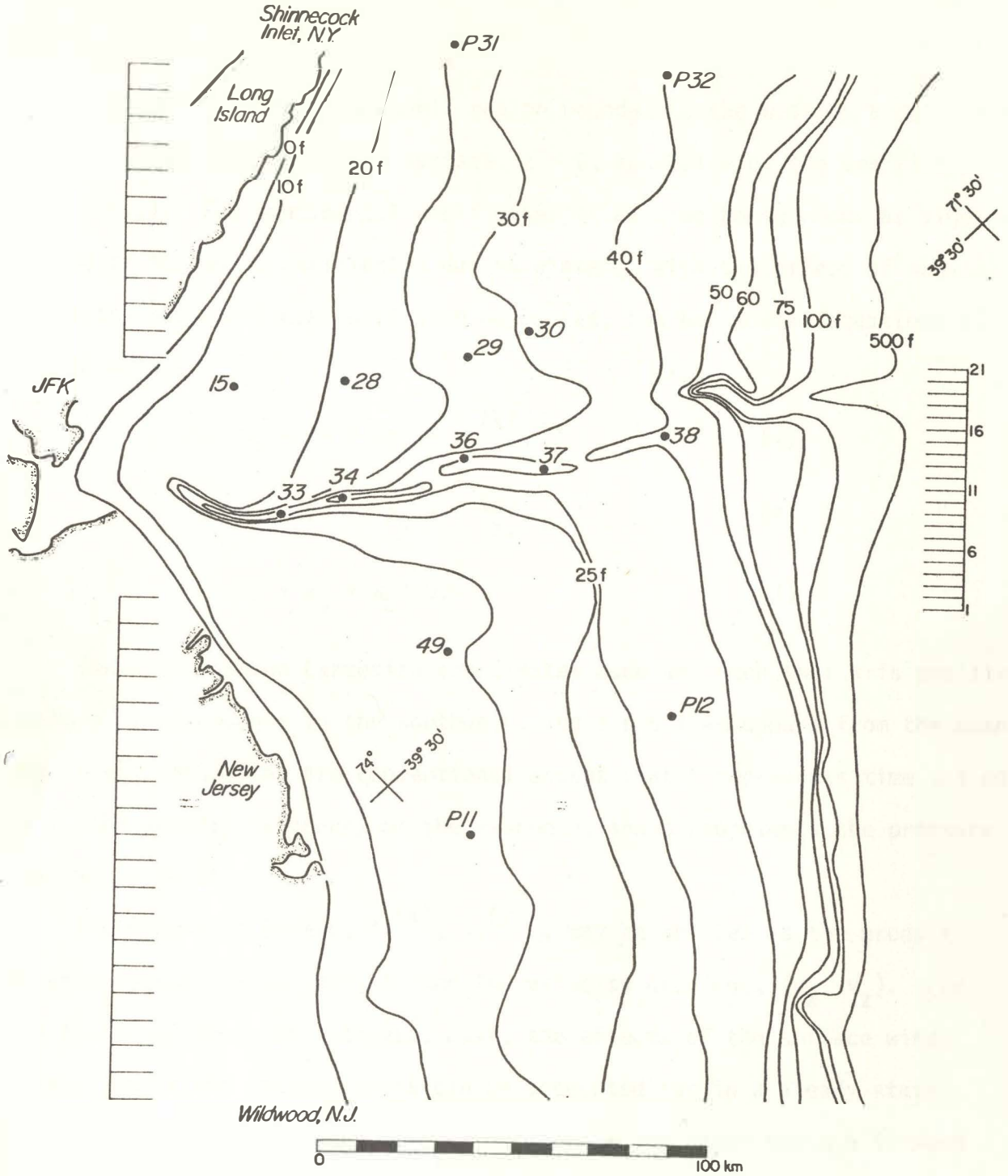

Fig. 1. The geography and bathymetry of the New York Bight area that falls within the model domain. The plot represents a clockwise rotation of 45° from the conventional map orientation. The staffs on the side mark the division of the area into three sections. From top to bottom, these are the Long Island shelf, the Hudson Shelf Valley (HSV) region, and the New Jersey shelf. The tick marks on the staff indicate the alongshore (y) position of cross-shelf (x-parallel) grid lines. The dots indicate current meter moorings during the 1975 Apex Gyre Outer Boundary (AGOB) experiment directed by the National Oceanic and Atmospheric Administration.

2. Formulation

Consider a continental shelf region bounded to the west by a coastline $x = X_2(y)$, above by the free surface, $z = 0$, and below by the sea floor, $z = -h(x,y)$. The continental-shelf water is assumed homogeneous as vigorous mixing by storms is anticipated during winter. With the effect of non-linearity and horizontal diffusion neglected, the horizontal equations of motion become

$$\omega\ u_t - fv = -p_x + \tau^{(x)}_z, \tag{1}$$

$$\omega\ v_t + fu = -p_y + \tau^{(y)}_z, \tag{2}$$

$$u_x + v_y + w_z = 0. \tag{3}$$

The right-handed Cartesian coordinates used are such that x is positive onshore, y alongshore to the southwest, and z positive upward from the mean sea level. Notations are conventional except that t represents time scaled by ω, the angular frequency of the response, and p represents the pressure divided by density.

The kinematic stress, $(\tau^{(x)}, \tau^{(y)})$, may be written as the product of an exchange coefficient, A, and the velocity gradient, (u_z, v_z). For the frequency range of interest, $\omega << f$, the effects of the surface wind stress and of the bottom stress can be accounted for in a steady-state Ekman problem (Brink, 1982). In regions where the water depth h is much greater than the Ekman depth, $(2A/f)^{\frac{1}{2}}$, it can be shown that the combined volume transport of the Ekman layers is simply

$$-f^{-1}\hat{k} \times \vec{\tau}_w + \delta_0(-\vec{v}^I + \hat{k} \times \vec{v}^I),$$

where $\vec{\tau}_w$ is the surface wind stress, $\vec{v}^I$ the geostrophic flow velocity, and

δ_o the scale thickness of the bottom Ekman layer.

The part of the expression that represents the contribution from the bottom Ekman layer is consistent with a more general formulation below that contains the veering angle, α, between $\vec{v}^I$ and the bottom stress $\vec{\tau}_B$:

$$\delta\ (-\vec{v}^I \sin\alpha + \hat{k} \times \vec{v}^I \cos\alpha),$$

where δ represents the displacement thickness of a turbulent bottom Ekman layer. When the flow is laminar, $\alpha = \pi/4$, and the simpler expression is recovered with $\delta_o = \delta \sin(\pi/4)$.

Estimates of α can be made from the complex correlation between pairs of near-bottom observations of currents (Kundu, 1976). Such estimates are made in the New York Bight during the period of interest at mooring sites 28, 33, 38 and 49. The results are presented in Table 1. Mayer et al. (1979) reported a veering angle of 28^o in the Ekman sense at mooring site 29 for fluctuating currents with a 3-day period on the basis of observations made in the winter of 1976. It appears that the estimates vary but the magnitude remains reasonably small. In the hindcast described later, α is thus set to zero, although, for the purpose of completeness, α is retained in the formulation.

The estimate of δ (or δ_o) is normally made on the assumption that friction to motions at synoptic frequencies arises due to turbulence generated by tidal currents at the sea floor. For a tidal current with a root-mean-square velocity of u_{rms}, the magnitude of the bottom stress exerted by the sea floor on the flow is approximately $C_D\ u_{rms}^2$, where C_D is a drag coefficient. In an Ekman layer that sustains a stress of this magnitude,

Table 1.

Estimates of α from 40 hr. low-passed velocity time series in the New York Bight

Current meter	Height above bottom (m)	Start time Julian day, 1975	Length of series (days)	α in Ekman sense	Correlation
28A	13.7	58.6	32	$-4^{o}.8$	0.81
28B	1.0	58.6	36		
33C	19.8	60.7	36	$18^{o}.0$	0.84
33D	1.0	60.7	28		
38B	35.1	57.5	59	$28^{o}.7$	0.87
38C	1.0	57.5	59		
49B	8.2	61.6	36	$-13^{o}.4$	0.64
49C	1.0	61.6	28		

the exchange coefficient A must be such that

$$\frac{A\, u_{rms}}{\delta_o} \sim C_D\, u_{rms}^2$$

Hence,

$$A \sim \delta_o\, C_D\, u_{rms}.$$

It then follows that

$$\delta_o \sim \frac{2\, C_D\, u_{rms}}{f}.$$

In the New York Bight, observations show that the velocity magnitude associated with the dominant M_2 -tide is 10 cm/sec (Mayer, Hansen, and Ortman, 1979). Consequently, for a drag coefficient of 2.5×10^{-3}, the thickness of the turbulent bottom Ekman layer is on the order of 5 m in the New York Bight. (A bottom Ekman layer thickness of 9.375 m is actually used in the hindcast for the circulation in the Long Island and New Jersey shelves, yielding results in good agreement with the observation. See Later.) The bottom Ekman layer thickness in the New York Bight is thus expected to be small compared to the depth of the continental shelf region to be modeled that ranges from 18 to 183 m (see later). The combined volume transport in the frictional layers is therefore adequately represented by:

$$\vec{Q}_F = -f^{-1}\, \hat{k} \times \vec{\tau}_w + \delta\, (-\vec{v}^I \sin\alpha + \hat{k} \times \vec{v}^I \cos\alpha). \quad (4)$$

With the parameterization of the kinematic stress, the system (1)-(3)

becomes deterministic in the sense that from it, an equation for the pressure alone can now be derived. Because of differences in bathymetry, the derivation of the pressure equation differs for different sections of the continental shelf in the New York Bight. (See Fig. 1 for section definition.) Over the Long Island and New Jersey shelves, the isobaths roughly run parallel to the coastline, making variations alongshore much more gradual than those across the shelf. As a consequence, to the zeroth order, (1) is reduced to the geostrophic balance and the derivation follows Hsueh and Lee (1978). The governing pressure equation in this case is as follows:

$$H\, p_{xxt} + H_x p_{xt} - f\, J(p, H) + f\delta p_{xx} \cos\alpha = f\, \hat{k} \cdot \nabla \times \vec{\tau}_w \,. \quad (5)$$

Here, the dominant dynamic feature is of course the well-known continental shelf waves (CSW). The time t, as well as the rest of the equation is now dimensional.

In the Hudson Shelf Valley (HSV) region, the isobaths turn and run shoreward across the continental shelf. The alongshore variations are no longer negligible and the velocity component offshore rivals that alongshore in magnitude. For low frequencies ($\omega << f$), the momentum balance to the zeroth order is thus geostrophic in both directions. For the pressure equation derivation in this case, it is convenient to introduce a regular perturbation in powers of ω/f. In the interior, away from frictional layers, the zeroth order approximation to (1)-(3) is as follows:

$$v^I_{(o)} = p_{(o)_x}$$

$$-u^I_{(o)} = p_{(o)_y},$$

$$w^I_{(o)} = 0.$$

The first order correction to the above is of course:

$$u^I_{(o)_t} - v^I_{(1)} = -p_{(1)_x},$$

$$v^I_{(o)_t} + u^I_{(1)} = -p_{(1)_y},$$

$$u^I_{(1)_x} + v^I_{(1)_y} + w^I_{(1)_z} = 0,$$

Here, the integer subscript in parentheses indicates the power of the smallness parameter in an expansion such as

$$u^I = u^I_{(o)} + (\tfrac{\omega}{f})\, u^I_{(1)} + (\tfrac{\omega}{f})^2\, u^I_{(2)} + \ldots, \text{ etc.}$$

The variables in the above expansions are all properly scaled according to various combinations of depth, length and velocity scales that are pertinent.

Before a vertical integration of (3) is performed to arrive at an

approximate equation for the pressure field, it is important to recognize that approximation to horizontal divergence $\nabla_H \cdot \vec{v}^I$ and topographic lifting $\vec{v}^I \cdot \nabla H$ must be obtained. The interior velocity to $O(\frac{\omega}{f})$ is given

$$\vec{v}^I = \hat{k} \times \nabla p_{(o)} + \frac{\omega}{f} \hat{k} \times \vec{v}^I_{(o)_t} + \frac{\omega}{f} \hat{k} \times \nabla p_{(1)}$$

The divergence is thus

$$\nabla_H \cdot \vec{v}^I = - \frac{\omega}{f} \hat{k} \cdot \nabla \times \vec{v}^I_{(o)_t} + 0 \left(\frac{\omega}{f}\right)^2.$$

The topographic lifting is given, to the first order, by

$$\vec{v}^I \cdot \nabla H = \hat{k} \times \nabla p_{(o)} \cdot \nabla H + \frac{\omega}{f} \left(\hat{k} \times \nabla p_{(1)} + \hat{k} \times \vec{v}^I_{(o)_t}\right) \cdot \nabla H.$$

Note here that in addition to ω/f, the alignment of the flow relative to the bathymetry enters as a factor. The first order flow is effective only when the flow is cross-isobath. For low-frequency barotropic flows on the continental shelf, the cross-isobath velocity is generally small, making the first-order flow contribution to lifting an second order effect. Thus to the lowest order,

$$\vec{v}^{I} \cdot \nabla H = \hat{k} \times \nabla p_{(o)} \cdot \nabla H.$$

Upon vertically integrating (3) and taking into account the above, it follows that in dimensional form,

$$H \nabla^2 p_t - f J (p, H) + f\delta \cos\alpha \nabla^2 p = f \hat{k} \cdot \nabla \times \vec{\tau}_w \quad (6)$$

where the subscript "(0)" is suppressed and J (p,H) stands for the Jacobian.

The main dynamic feature in (6) is the quasi-geostrophic topographical Rossby wave (TRW), to the equation of which it reduces when δ and $\vec{\tau}_w$ are set to zero.

The circulation in the New York Bight is thus describable in three longshore regimes: (a) the upstream CSW regime over the Long Island shelf where (5) applies, (b) the TRW regime over the HSV where (6) prevails, (c) the downstream CSW regime over the New Jersey shelf where (5) is again in force. Within each of these shelf sections, the appropriate pressure equation is integrated numerically seaward to the 100-fathom isobath where an adiabetic condition (p=0) is enforced. Inshore, a no-normal transport condition is applied at the coast, which, for the CSW-dominated sections, coincides with the 10-fathom isobath, and for the HSV region, is replaced for simplicity with a hypothetical zero-depth contour that is parallel to the y-axis. To the same order of approximation as is in (5) and (6), these conditions are respectively:

$$\hat{n} \times \hat{k} \cdot [(H - \delta \sin\alpha)\nabla p + \hat{j}\, Hf^{-1} p_{xt} - \vec{\tau}_w] - \hat{n} \cdot (\delta \cos\alpha)\nabla p = 0, \qquad (7)$$

and

$$\hat{n} \times \hat{k} \cdot \vec{\tau}_w - \hat{n} \times \hat{k} \cdot (\delta \sin\alpha)\nabla p - \hat{n} \cdot (\delta \cos\alpha)\nabla p = 0, \qquad (8)$$

where $\hat{j}$ is the unit vector along the y-axis and $\hat{n}$ an offshore-directed unit vector normal to the coastline.

The continuity of pressure along common (x-parallel) grid lines is required as a matching conditon between sections. Judicial placement (20 km offshore of the John F. Kennedy airport) of the zero-depth contour in the HSV region and the naturally small separation (about equal to or less than one grid interval in the x-direction) between the 0-fathom and 10-fathom isobaths in the New York Bight ensures proper matching of the pressure nearshore, where pressure calculated over one depth in the CSW-dominated section is applied as prescribed pressure over another depth in the HSV region where the dynamics is TRW-dominated and vice versa. The depth mismatch extends offshore only to the 20-fathom isobath, beyond which the model isobaths run very close geographically to their counterparts in the CG&S charts. Surface winds observed at the John F. Kennedy airport are used to establish, through a bulk aerodynamical formula, the forcing wind-stress field. Since winds at one location only is used, the curl of the established wind-stress field is zero. As a consequence, (5) and (6) are both homogeneous and the local wind forcing enters in the no-normal transport condition only.

In addition to local winds, the composite model of the New York Bight

is also forced by the flow on the continental shelf upstream from the Long Island section. This upstream flow condition is formulated as a prescribed cross-shelf pressure distribution that is in geostrophic balance with observed longshore currents at mooring stations P31 and P32. The numerical integration for the composite model thus proceeds with finding the solution to (5) for the Long Island continental shelf (10-fathom isobath to 100-fathom isobath) from the P31-P32 line to just below the HSV. Although longshore currents observed at mooring stations, 28, 29, and 30 are well-accounted for by the upstream CSW-solution, as expected, the flow in the HSV is grossly misrepresented particularly in phase. To reproduce the observed HSV flow, numerical solution to (6) instead is sought that matches the CSW pressure along a transect just upstream from mooring station 28. This integration of (6) extends downstream to another transect 13 km upstream from mooring station 49, along which the dominance of the CSW-dynamics is expected to begin anew. Downstream from this latter transect, an integration procedure similar to that for the Long Island shelf is applied to the New Jersey continental shelf to a point near Wildwood, New Jersey.

As (5) is parabolic in nature, no cross-shelf boundary condition is needed on the downstream limit for both the Long Island and New Jersey computations. For the HSV region, since (6) is elliptic, a downstream cross-shelf boundary condition must be prescribed. A condition that has been adequate for the steady-state study cited earlier is the vanishing of the second y-derivative, $p_{yy} = 0$. This condition is again used in the present HSV computation and it now reads, in accordance with (6):

$$Hp_{xxt} - fJ(p,H) + f\delta p_{xx} \cos \alpha = 0. \qquad (9)$$

3. Numerical Model

The integration of (5) and (6) over their respective domains of applicability is carried out numerically on a main-frame electronics computer. To simplify the calculation, the irregular shape of the horizontal domain of integration is transformed into a rectangle through the use of the following coordinate transformation:

$$x^* = \frac{x - X_1}{X},$$

$$y^* = y,$$

where $X = X_2 - X_1$, the local width of the continental shelf. The shelf break at the 100-fathom isobath is represented here by $x = X_1(y)$. In the new coordinates, both the coastline ($x^* = 1$) and the shelf break ($x^* = 0$) are straight lines and the cross-shelf grid-interval remains a constant fraction (0.05) of local shelf width. The model resolution in the cross-shelf direction is thus higher over sections of the shelf where the width is smaller.

The transformed pressure equations and boundary conditions for the two types of computational region for a vanishing veering angle ($\alpha = 0$) are as follows:

For regions in which (5) and (7) apply:

$$\frac{H}{fX} p_{xxt} + \frac{H_x}{fX} p_{xt} + H_x p_y - H_y p_x + \frac{\delta}{X} p_{xx} = 0,$$

$$\frac{H}{fX} p_{xt} + \frac{\delta}{X} [(X_2')^2 + 1] p_x + (H - \delta X_2') p_y = \tau_w^y + X_2' \tau_w^x, \quad x = 1 \text{ (coast)},$$

$$p = 0,\ x = 0 \text{ (shelf break)},$$

$$p\ (x,o,t) \text{ specified.}$$

For the region in which (6) and (8) apply:

$$H\left(\frac{1}{X^2} + F^2\right) p_{xxt} + H\left(FF_x + F_y\right) p_{xt} + 2HFp_{xyt} + Hp_{yyt}$$

$$+ \frac{f}{X}\left(H_x p_y - H_y p_x\right) + f\delta\left\{\left(\frac{1}{X^2} + F^2\right) p_{xx} + \left(FF_x + F_y\right) p_x + 2Fp_{xy} + p_{yy}\right\} = 0,$$

$$\frac{\delta}{X}\left[\left(X_1'\right)^2 + 1\right] p_x - \delta X_1' p_y = \tau_w^y + X_1' \tau_w^x,\ x = 0 \text{ (coast of zero depth)},$$

$$p = 0,\ x = 1 \text{ (shelf break)},$$

$p(x,t)$ specified along the upstream (Long Island side) cross-shelf boundary,

$$H p_{xxt} + fX\left(H_x p_y - H_y p_x\right) + f\delta P_{xx} = 0, \text{ along the downstream}$$

(New Jersey side) cross-shelf boundary.

In the above, the asterisks have been dropped from the transformed coordinates, τ_w^x and τ_w^y represent respectively the x- and y-components of the wind stress and the function F emerges from derivative transformation and is given by

$$F = -\left(xX' + X_1'\right)/X.$$

Note also that, in the HSV region, the coordiantes are reversed relative to those described earlier. The transformed x-coordinate is here directed

offshore from the coast where x = 0 to the shelf break where x = 1 and the y-coordinate is directed from the New Jersey end of the shelf toward the Long Island. In the untransformed coordinates, $x = X_1(y)$ gives, in the HSV region, the coastline instead and the shelf break is given by $x = X_2(y)$.

The pressure equations and boundary conditions are cast in dimensionless forms and are discretized over space and time in intended regions. As the nondimensionalization and discretization differ between the CSW-dominated region and the region in which TRW is dominating, in what follows, separate descriptions of these procedures will be made for each region.

Long Island and New Jersey shelves

The variables are nondimensionalized in the CSW-dominated regions according to the following scheme:

$$(\delta, H) = H_o(\tilde{\delta}, \tilde{H}),\ X = L\tilde{X},\ y = Y\tilde{y},\ t = \omega^{-1}\tilde{t},\ \ p = fVL\tilde{p},\ (\tau_w^x, \tau_w^y) = \tau_o\,(\tilde{\tau}_w^x, \tilde{\tau}_w^y).$$

As the cross-shelf distance is already in fractions, no scaling is necessary for x.

The transformed (5) in its dimensionless form can thus be written as:

$$(\tfrac{\omega Y}{fL})\,\tfrac{1}{X}\,(Hp_{xxt} + H_x p_{xt}) + H_x p_y - H_y p_x + (\tfrac{Y}{L})\tfrac{\delta}{X} p_{xx} = 0$$

The accompanying coastal boundary condition is:

$$(\tfrac{\omega Y}{fL})\,\tfrac{H}{X}\,p_{xt} - (\tfrac{Y}{L})\tfrac{\delta}{X}\,[(\tfrac{L}{Y})^2\,(X_2')^2 + 1]p_x + [(\tfrac{L}{Y})X_2'\delta - H]p_y = [-\tau_w^y - (\tfrac{L}{Y})X_2'\,\tau_w^x]\cdot\tfrac{\tau_o Y}{fVLH_o},$$

The upstream condition must also be scaled accordingly before it is applied.

Except for L/Y the nondimensional ratios that appear in the above equations can all be made to be unity by a judicial choice of the scales. In the New York Bight area a median value of the Coriolis parameter f is 9.375×10^{-5} sec^{-1}. For $\tau_o = 1$ dyne cm^{-2}, V = 10 cm sec^{-1}, L = 10^7cm, and $H_o = 10^4$cm, such a reduction to unity is achieved with Y = 937.5 km, δ = 9.375 m, and $\omega = 9.375 \times 10^{-6}$ sec^{-1}. With this choice of scales, the model equations are thus:

$$Hp_{xxt} + H_x p_{xt} + X H_x p_y - XH_y p_x + p_{xx} = 0, \qquad (10)$$

$$\frac{H}{X} p_{xt} + [(\frac{L}{Y})^2 (X_2')^2 + 1]p_x - [(\frac{L^2}{Y})\delta X_2' - H]p_y = \tau_w^y + (\frac{L}{Y})X_2' \tau_w^x, \; x = 1, \qquad (11)$$

To discretize (10) and (11), the following finite-differencing scheme is introduced:

$$X_{j+\frac{1}{2}} = \tfrac{1}{2} (X_{j+1} + X_j)$$

$$H_{i,j+\frac{1}{2}} = \tfrac{1}{2} (H_{i,j+1} + H_{i,j})$$

$$(H_x)_{i,j+\frac{1}{2}} = \frac{1}{4\Delta x} (H_{i+1,j+1} - H_{i-1,j+1} + H_{i+1,j} - H_{i-1,j})$$

$$(H_y)_{i,j+\frac{1}{2}} = \frac{1}{\Delta y} (H_{i,j+1} - H_{i,j})$$

$$(X_2')_{j+\frac{1}{2}} = \frac{1}{\Delta y} [(X_2)_{j+1} - (X_2)_j]$$

$$(p_y)^{n+\frac{1}{2}}_{i,j+\frac{1}{2}} = \frac{1}{2\Delta y}\ (p^{n+1}_{i,j+1} - p^{n+1}_{i,j} + p^{n}_{i,j+1} - p^{n}_{i,j})$$

$$(p_x)^{n+\frac{1}{2}}_{i,j+\frac{1}{2}} = \frac{1}{8\Delta x}\ (p^{n+1}_{i+1,j} - p^{n+1}_{i-1,j} + p^{n+1}_{i+1,j+1} - p^{n+1}_{i-1,j+1} + p^{n}_{i+1,j} - p^{n}_{i-1,j} + p^{n}_{i+1,j+1} - p^{n}_{i-1,j+1})$$

$$(p_{xx})^{n+\frac{1}{2}}_{i,j+\frac{1}{2}} = \frac{1}{4\Delta x^2}\ (p^{n+1}_{i+1,j} + p^{n+1}_{i-1,j} - 2p^{n+1}_{i,j} + p^{n+1}_{i+1,j+1} + p^{n+1}_{i-1,j+1} - 2p^{n+1}_{i,j+1} + p^{n}_{i+1,j} + p^{n}_{i-1,j} - 2p^{n}_{i,j} + p^{n}_{i+1,j+1} + p^{n}_{i-1,j+1} - 2p^{n}_{i,j+1})$$

$$(p_{xt})^{n+\frac{1}{2}}_{i,j+\frac{1}{2}} = \frac{1}{4\Delta x\Delta t}\ (p^{n+1}_{i+1,j} - p^{n+1}_{i-1,j} - p^{n}_{i+1,j} + p^{n}_{i-1,j} + p^{n+1}_{i+1,j+1} - p^{n+1}_{i-1,j+1} - p^{n}_{i+1,j+1} + p^{n}_{i-1,j+1})$$

$$(p_{xxt})^{n+\frac{1}{2}}_{i,j+\frac{1}{2}} = \frac{1}{2\Delta x^2\Delta t}\ (p^{n+1}_{i+1,j} + p^{n+1}_{i-1,j} - 2p^{n+1}_{i,j} - p^{n}_{i+1,j} - p^{n}_{i-1,j} + 2p^{n}_{i,j} + p^{n+1}_{i+1,j+1} + p^{n+1}_{i-1,j+1} - 2p^{n+1}_{i,j+1} - p^{n}_{i+1,j+1} - p^{n}_{i-1,j+1} + 2p^{n}_{i,j+1})$$

In the above, i and j are indices that mark a point of computation in integer number of grid intervals from the origin in, respectively, the x and y directions, and n marks the time of computation in integer number of time steps from the beginning. The finite difference is centered in the x direction

and forward in both y and t. Variables and x-derivatives are y- and t-averaged. Averages and forward differences in y and t are marked, respectively, by the subscript $j + \frac{1}{2}$ and superscript $n + \frac{1}{2}$. The grid interval in the x-direction, Δx, is set at 0.05; in dimensional terms, Δx ranges from 5.25 to 9.05 km through the entire New York Bight. The grid interval Δy is 0.007, or, dimensionally, 6.57 km on the two shelves over which CSW is dominating. The time step Δt is chosen to be 0.010125, or 18 minutes, in accordance with the Courant-Friedrichs-Levy condition. Experiments with smaller time steps show little difference in results.

In finite difference form, (10) becomes

$$(D + C - B + G)p^{n+1}_{i+1,j+1} + (A - 2C - 2G)p^{n+1}_{i,j+1} + (-D + C + B + G)p^{n+1}_{i-1,j+1}$$

$$= (DD)_{i,j} + (DDS)_{i,j}, \qquad (12)$$

where

$$G = H_{i,j+\frac{1}{2}}/2\Delta x^2 \, \Delta t$$

$$D = (H_x)_{i,j+\frac{1}{2}}/4\Delta x \, \Delta t$$

$$B = X_{j+\frac{1}{2}} \, (H_y)_{i,j+\frac{1}{2}}/8 \, \Delta x$$

$$C = 1/4 \, \Delta x^2$$

$$A = X_{j+\frac{1}{2}} \, (H_x)_{i,j+\frac{1}{2}}/2 \, \Delta y$$

$$(DD)_{i,j} = -G\,(p^{n+1}_{i+1,j} + p^{n+1}_{i-1,j} - 2p^{n+1}_{i,j}) - D\,(p^{n+1}_{i+1,j} - p^{n+1}_{i-1,j}) + Ap^{n+1}_{i,j}$$

$$+ B\,(p^{n+1}_{i+1,j} - p^{n+1}_{i-1,j}) - C\,(p^{n+1}_{i+1,j} + p^{n+1}_{i-1,j} - 2p^{n+1}_{i,j})$$

$$(DDS)_{i,j} = -G\,(-p^{n}_{i+1,j} - p^{n}_{i-1,j} + 2p^{n}_{i,j} - p^{n}_{i+1,j+1} - p^{n}_{i-1,j+1} + 2p^{n}_{i,j+1})$$

$$-D\,(-p^{n}_{i+1,j} + p^{n}_{i-1,j} - p^{n}_{i+1,j+1} + p^{n}_{i-1,j+1}) - A\,(p^{n}_{i,j+1} - p^{n}_{i,j})$$

$$+B\,(p^{n}_{i+1,j} - p^{n}_{i-1,j} + p^{n}_{i+1,j+1} - p^{n}_{i-1,j+1})$$

$$-C\,(p^{n}_{i+1,j} + p^{n}_{i-1,j} - 2p^{n}_{i,j} + p^{n}_{i+1,j+1} + p^{n}_{i-1,j+1} - 2p^{n}_{i,j+1}).$$

The no-flux condition (11) becomes

$$BAA(j)p^{n+1}_{NB+1,j+1} + BBB\,(j)p^{n+1}_{NB,j+1} + BCC(j)p^{n+1}_{NB-1,j+1} = FB(j), \quad (13)$$

where

$$BAA(j) = BTX + BC(j)$$

$$BBB(j) = -BY(j)$$

$$BCC(j) = -BAA(j)$$

$$BTX = 1/4\Delta x\Delta t$$

$$BC(j) = \{[(X_2')^2_{j+\frac{1}{2}}\,(\tfrac{L}{Y})^2 + 1\} \,/\, 8\Delta x\, H_{NB,j+\frac{1}{2}}$$

$$BY(j) = X_{j+\frac{1}{2}}\,\{(\tfrac{L}{Y})^2\,(X_2')_{j+1} - H_{NB,j+\frac{1}{2}}\} \,/ 2\Delta y\, H_{NB,j+\frac{1}{2}}$$

$$FB(j) = TBC(j) - BTX\ (p^{n+1}_{NB+1,j} - p^{n+1}_{NB-1,j} - p^{n}_{NB+1,j} + p^{n}_{NB-1,j} - p^{n}_{NB+1,j+1}$$

$$+ p^{n}_{NB-1,j+1}) - BC(j)\ (p^{n+1}_{NB+1,j} - p^{n+1}_{NB-1,j} + p^{n}_{NB+1,j} - p^{n}_{NB-1,j}$$

$$+ p^{n}_{NB+1,j+1} - p^{n}_{NB-1,j+1})$$

$$+ BY(j)\ (-p^{n+1}_{NB,j} + p^{n}_{NB,j+1} - p^{n}_{NB,j})$$

$$TBC(j) = [(\tau^{y}_{w})^{n+1} + (\tau^{y}_{w})^{n}]/2 + (\tfrac{L}{Y})\ (X'_2)_{j+\frac{1}{2}}\ [(\tau^{x}_{w})^{n+1} + (\tau^{x}_{w})^{n}]/2$$

The tri-diagonal nature of the (12) and (13) suggests solution by the use of a recurrence relation:

$$p^{n+1}_{i,j+1} = E_{i,j+1}\ p^{n+1}_{i+1,j+1} + F_{i,j+1}, \qquad (14)$$

where $E_{i,j+\frac{1}{2}}$ and $F_{i.j+1}$ are coefficients yet to be determined.

The determination of these coefficients is by way of a substitution, based on (14), for $p^{n+1}_{i-1,j+1}$ in (12). In terms of the other surviving pressure terms, (12) may thus be written as follows:

$$p^{n+1}_{i,j+1} = \frac{(AA)_i}{(BB)_i - (CC)_i\ E_{i-1,j+1}}\ p^{n+1}_{i+1,j+1} + \frac{(DD)_{i,j} + (DDS)_{i,j} + (CC)_i F_{i-1,j+1}}{(BB)_i - (CC)_i\ E_{i-1,j+1}}, \qquad (15)$$

where

$$(AA)_i = -(D + C - B + G),$$

$$(BB)_i = A - 2C - 2G,$$

$$(CC)_i = -(-D + C + B + G).$$

By comparing (15) with (14), it is plain that

$$E_{i,j+1} = \frac{(AA)_i}{(BB)_i - (CC)_i E_{i-1,j+1}}, \tag{16}$$

$$F_{i,j+1} = \frac{(DD)_{i,j} + (DDS)_{i,j} + (CC)_i F_{i-1,j+1}}{(BB)_i - (CC)_i E_{i-1,j+1}} \tag{17}$$

Since the pressure is zero at the shelf break (i=1), (14) implies that

$$E_{1,j+1} = 0, \quad F_{1,j+1} = 0.$$

With this adiabetic condition, the recurrence relations (16) and (17) thus complete the determination of the E's and F's over the entire shelf.

In particular, the E's and F's along the coast (i=NB) are now known also. Upon eliminating p_{NB-1} and p_{NB+1} from (13) by use of the recurrence relation (14), it follows that

$$p^{n+1}_{NB,j+1} = \frac{FB(j) + \dfrac{BAA(j)}{E_{NB,j+1}} F_{NB,j+1} - BCC(j) \cdot F_{NB-1,j+1}}{\dfrac{BAA(j)}{E_{NB,j+1}} + BBB(j) + BCC(j) \cdot E_{NB,j+1}}. \qquad (18)$$

With pressure along the coast thus determined, the pressure field over the entire shelf can be obtained from (15). The interior velocity is computed from the calculated pressure field according to the following approximation to (1) and (2):

$$fv = p_x,$$

$$v_t + fu = -p_y$$

In transformed coordinates, these become:

$$fv = \frac{1}{X} p_x$$

$$v_t + fu = -p_y + (xX' + X'_1)\, p_x/X$$

In dimensionless form, these yield

$$v = \frac{1}{X} p_x, \qquad (19a)$$

$$u = -\left(\frac{L}{Y}\right) \left\{\frac{1}{X} p_{xt} + p_y - \frac{xX' + X'_1}{X} p_x\right\}, \qquad (19b)$$

where u and v are scaled with the velocity scale V (=10 cms^{-1}).

From the finite difference forms of (19a)and (19b) horizontal velocity components at each grid point are calculated from the known pressure field. The calculated values of the velocity components represent a model prediction for currents in the synoptic band away from frictional boundary layers. Comparisons later to near-bottom direct current measurements show good agreement between the prediction and observation.

Hudson Shelf Valley (HSV)

In the HSV region, the nondimensionalization scheme remain the same except that there is no longer any distinction between the horizontal length scales. L (=10^7cm) suffices as the lone scale for the horizontal distance and δ the bottom boundary thickness is taken dimensionally to be 5 m. In its dimensionless form, the transformed (6) reads:

$$\delta\left(\frac{1}{X^2} + F^2\right)p_{xx} - \left\{\frac{H_Y}{X} - \delta(FF_x + F_y)\right\} p_x + 2\delta F p_{xy} + \frac{H_x}{X} p_y + \delta p_{yy} + \varepsilon H\left(\frac{1}{X^2} + F^2\right)p_{xxt}$$

$$+ \varepsilon H(FF_x + F_y)p_{xt} + 2\varepsilon HF p_{xyt} + \varepsilon H p_{yyt} = 0, \qquad (20)$$

where $\varepsilon = \omega/f$.

The no-flux condition at the coast (x = o):

$$\frac{\delta}{X}\left[(X_1')^2 + 1\right]p_x - \delta X_1' p_y = \tau_w^y + X_1'\tau_w^x,$$

where τ_o is chosen to be 9.375 dyn cm^{-2}.

As is mentioned in Section 2, the model coast for the HSV region is a straight line parallel to the y-axis. For such a coastline, $X_1' = 0$, and the no-flux condition reduces to

$$p_x = \frac{X}{\delta} \tau_w^y. \qquad (21).$$

The condition along the cross-shelf transect that forms the downstream limit of the HSV region is now:

$$\varepsilon H p_{xxt} + X(H_y p_x - H_x p_y) + \delta p_{xx} = 0 \qquad (22)$$

After rearranging (20) may be written as follows:

$$p_{xx} + Ap_{yy} + Bp_{xy} + Cp_x + Dp_y + EEp_{xt} + EGp_{xxt} + EKp_{xyt} + EFp_{yyt} = 0, \quad (23)$$

where

$$A = \delta/A'$$

$$A' = \delta\left(\frac{1}{X^2} + F^2\right)$$

$$B = 2\delta F/A'$$

$$C = -\left[\frac{H_y}{X} - \delta(FF_x + F_y\right]/A'$$

$$D = H_x/XA'$$

$$EE = \varepsilon H(FF_x + F_y)/A'$$

$$EG = \varepsilon H(\frac{1}{X^2} + F^2)/A'$$

$$EK = 2\varepsilon HF/A'$$

$$EF = \varepsilon H/A'$$

To discretize (20)-(22), a finite difference centered in x and y and forward in time is adopted. Again, variables and spatial derivatives are time-averaged to enhance computational stability. In its finite difference form, (20) may be rearranged to be:

$$(1 + \frac{\Delta x}{2} C_{ij} + \frac{\Delta x}{\Delta t} EE_{ij} + \frac{2}{\Delta t} EG_{ij})p^{n+1}_{i+1,j} + (\frac{\Delta x}{4\Delta y} B_{ij} + \frac{\Delta x}{2\Delta y \Delta t} EK_{ij})p^{n+1}_{i+1,j+1}$$

$$-(\frac{\Delta x}{4\Delta y} B_{ij} + \frac{\Delta x}{2\Delta y \Delta t} EK_{ij})p^{n+1}_{i+1,j-1} -2[1 +(\frac{\Delta x}{\Delta y})^2 A_{ij} + \frac{2}{\Delta t} EG_{ij} + \frac{2}{\Delta t}(\frac{\Delta x}{\Delta y})^2 EF_{ij}]p^{n+1}_{i,j}$$

$$+[(\frac{\Delta x}{\Delta y})^2 A_{ij} + \frac{\Delta x^2}{2\Delta y} D_{ij} + \frac{2}{\Delta t}(\frac{\Delta x^2}{\Delta y}) EF_{ij}]p^{n+1}_{i,j+1} + [(\frac{\Delta x}{\Delta y})^2 A_{ij} - \frac{\Delta x^2}{2\Delta y} D_{ij} + \frac{2}{\Delta t}(\frac{\Delta x}{\Delta y})^2 EF_{ij}]p^{n+1}_{i,j-1}$$

$$+(1 - \frac{\Delta x}{2} C_{ij} - \frac{\Delta x}{\Delta t} EE_{ij} + \frac{2}{\Delta t} EG_{ij})p^{n+1}_{i-1,j} - (\frac{\Delta x}{4\Delta y} B_{ij} + \frac{\Delta x}{2\Delta y \Delta t} EK_{ij})p^{n+1}_{i-1,j+1}$$

$$+(\frac{\Delta x}{4\Delta y} B_{ij} + \frac{\Delta x}{2\Delta y \Delta t} EK_{ij})p^{n+1}_{i-1,j-1} = - (1 + \frac{\Delta x}{2} C_{ij} - \frac{\Delta x}{\Delta t} EE_{ij} - \frac{2}{\Delta t} EG_{ij})p^{n}_{i+1,j}$$

$$-(\frac{\Delta x}{4\Delta y} B_{ij} - \frac{\Delta x}{2\Delta y \Delta t} EK_{ij})p^{n}_{i+1,j+1} + (\frac{\Delta x}{4\Delta y} B_{ij} - \frac{\Delta x}{2\Delta y \Delta t} EK_{ij})p^{n}_{i+1,j-1}$$

$$+ 2[1 + (\frac{\Delta x}{\Delta y})^2 A_{ij} - \frac{2}{\Delta t} EG_{ij} - \frac{2}{\Delta t}(\frac{\Delta x}{\Delta y})^2 EF_{ij}]p^n_{i,j} - [(\frac{\Delta x}{\Delta y})^2 A_{ij} + \frac{\Delta x^2}{2\Delta y} D_{ij} - \frac{2}{\Delta t}(\frac{\Delta x}{\Delta y})^2 EF_{ij}]p^n_{i,j+1}$$

$$-[(\frac{\Delta x}{\Delta y})^2 A_{ij} - \frac{\Delta x^2}{2\Delta y} D_{ij} - \frac{2}{\Delta t}(\frac{\Delta x}{\Delta y})^2 EF_{ij}]p^n_{i,j-1} - (1 - \frac{\Delta x}{2} C_{ij} + \frac{\Delta x}{\Delta t} EE_{ij} - \frac{2}{\Delta t} EG_{ij})p^n_{i-1,j}$$

$$+(\frac{\Delta x}{4\Delta y} B_{ij} - \frac{\Delta x}{2\Delta y \Delta t} EK_{ij})p^n_{i-1,j+1} - (\frac{\Delta x}{4\Delta y} B_{ij} - \frac{\Delta x}{2\Delta y \Delta t} EK_{ij})p^n_{i-1,j-1}. \quad (23)$$

In the above, A_{ij}, etc. are values of the coefficients at the grid point $(i\Delta x, j\Delta y)$. In the HSV region, Δx remains 0.05 of the local shelf width. Here, Δx ranges from 7.75 km to 8.6 km dimensionally. The alongshore grid interval is reduced by nearly half from that used in the CSW regions to 3.475 km. The increased resolution is necessary for the representation of sharp alongshore variations in bathymetry encountered in the HSV. As a consequence, the time step, Δt, is also reduced to 0.0028125, 5 minutes, to maintain computational stability.

The downstream condition (22) (applied at j=1) can be similarly discretized. The resulting finite difference equation is as follows:

$$[(H)_{i,1} \frac{2\varepsilon}{\delta \Delta t} + 1 - (\frac{HX_y}{\delta})_{i,1} \frac{\Delta x}{2}]p^{n+1}_{i+1,1} - [(\frac{XH_x}{\delta})_{i,1} \frac{\Delta x^2}{\Delta y} + 2 + (H)_{i,1} \frac{4\varepsilon}{\delta \Delta t}]p^{n+1}_{i,1}$$

$$(\frac{XH_x}{\delta})_{i,1} \frac{\Delta x^2}{\Delta y} p^{n+1}_{i,2} + [(H)_{i,1} \frac{2\varepsilon}{\delta \Delta t} + (\frac{XH_y}{\delta})_{i,1} \frac{\Delta x}{2} + 1]p^{n+1}_{i-1,1}$$

$$= [(H)_{i,1} \frac{2\varepsilon}{\delta \Delta t} + (\frac{XH_y}{\delta})_{i,1} \frac{\Delta x}{2} - 1]p^n_{i+1,1} - [(H)_{i,1} \frac{4\varepsilon}{\delta \Delta t} - (\frac{XH_y}{\delta})_{i,1} \frac{\Delta x^2}{\Delta y} - 2]p^n_{i,1}$$

$$- (\frac{XH_x}{\delta})_{i,1} \frac{\Delta x^2}{\Delta y} p^n_{i,2} + [(H)_{i,1} \frac{2\varepsilon}{\delta \Delta t} - (\frac{XH_y}{\delta})_{i,1} \frac{\Delta x}{2} - 1]p^n_{i-1,1}, \quad (24)$$

where centered difference is implied and no y-average is employed.

Since cross-shelf pressure distribution calculated for the Long Island shelf is imposed upstream, the upstream boundary condition is simply

$$p^{n+1}_{i,M} = FP(i,M), \qquad (25)$$

where j=M marks the upstream cross-shelf boundary to the TRW calculation.

The no-flux condition (21) at the coast (i=1) in finite difference form is simply:

$$p^{n+1}_{2,j} - p^{n+1}_{i,j} = \left(\frac{X\Delta x}{\delta}\tau^{y}_{w}\right)_j, \qquad (26)$$

where the derivative in x is one-sided and for simplicity, not time-averaged.

For a given offshore location (fixed i), (23)-(26) describes the constraint on pressure at each of the alongshore (j) grid points. It is therefore convenient to represent pressure values at each j as components of a column vector as follows:

$$f^{n+1}_{i} = \text{Col}\ \{p^{n+1}_{i,1}, p^{n+1}_{i,2}, \text{---}, p^{n+1}_{i,M}\}$$

For interior offshore locations (excluding the ones at the coast, i=1, and the shelf break, i=N), (23)-(25) can be combined in a matrix equation:

$$\tilde{A}\, f^{n+1}_{i-1} + \tilde{B}\, f^{n+1}_{i} + \tilde{C}\, f^{n+1}_{i+1} = D. \qquad (27)$$

For points along the coast, (26) gives

$$\tilde{A}_b \, f_1^{n+1} + \tilde{B}_b \, f_2^{n+1} = D_b. \qquad (28)$$

Along the shelf break, the adiabetic condition means, of course,

$$f_N^{n+1} = 0. \qquad (29)$$

The coefficient matrices, $\tilde{A}$, etc., are M x M matrices whose elements are coefficients to the unknown pressure terms at time step n+1. The D's are column vectors that contain the known terms on the righ-hand side of (23)-(26), (The dimension of D and D_b is the same as that of f_i, namely M.)

The none-zero membership for $\tilde{A}$ is thus:

$$\left.\begin{aligned} A_{1,1} &= 1 + \left(-\frac{XH_y}{\delta}\right)_{i,1} \frac{\Delta x}{2} + H_{i,1} \frac{2E}{\delta \Delta t} \\ A_{j,1} &= 1 - \frac{\Delta x}{2} C_{ij} - \frac{\Delta x}{\Delta t} EE_{ij} + \frac{2}{\Delta t} EG_{ij} \\ A_{i,j+1} &= -\frac{\Delta x}{4 \Delta y} B_{ij} - \frac{\Delta x}{2 \Delta y \Delta t} EK_{ij} \\ A_{j,j-1} &= -A_{j,j+1} \end{aligned}\right\}, \qquad (30)$$

where the first subscript to A indicates row number and the second indicates column member of the matrix element. The range of i is 2 to N-1 and that of j, 1 to M-1.

For $\tilde{B}$, for the same index range,

$$\left.\begin{aligned}
B_{1,1} &= -\left[2 + \left(\frac{XH_x}{\delta}\right)_{i,1}\frac{\Delta x^2}{\Delta y} + H_{i,1}\frac{4\varepsilon}{\delta\Delta t}\right] \\
B_{1,2} &= \left(\frac{XH_x}{\delta}\right)_{i,1}\frac{\Delta x^2}{\Delta y} \\
B_{j,j} &= -2\left[1 + \left(\frac{\Delta x}{\Delta y}\right)^2 A_{ij} + \frac{2}{\Delta t}EG_{ij} + \frac{2}{\Delta t}\left(\frac{\Delta x}{\Delta y}\right)^2 EF_{ij}\right] \\
B_{j,j+1} &= \left(\frac{\Delta x}{\Delta y}\right)^2 A_{ij} + \frac{\Delta x^2}{2\Delta y}D_{ij} + \frac{2}{\Delta t}\left(\frac{\Delta x}{\Delta y}\right)^2 EF_{ij} \\
B_{j,j-1} &= \left(\frac{\Delta x}{\Delta y}\right)^2 A_{ij} - \frac{\Delta x^2}{2\Delta y}D_{ij} + \frac{2}{\Delta t}\left(\frac{\Delta x}{\Delta y}\right)^2 EF_{ij} \\
B_{M,M} &= 1
\end{aligned}\right\} \quad (31)$$

Similarly, for $\tilde{C}$,

$$\left.\begin{aligned}
C_{1,1} &= -\left(\frac{XH_x}{\delta}\right)_{i,1}\frac{\Delta x}{2} + 1 + H_{i,1}\frac{2\varepsilon}{\delta\Delta t} \\
C_{j,j} &= 1 + \frac{\Delta x}{2}C_{ij} + \frac{\Delta x}{\Delta t}EE_{ij} + \frac{2}{\Delta t}EG_{ij} \\
C_{j,j+1} &= \frac{\Delta x}{4\Delta y}B_{ij} + \frac{\Delta x}{2\Delta y\Delta t}EK_{ij} \\
C_{j,j-1} &= -C_{j,j+1}
\end{aligned}\right\} \quad (32)$$

The components of the column vector are given by the following:

$$
\left.
\begin{aligned}
D_1 &= [H_{i,1}\frac{2\varepsilon}{\delta\Delta t} + (\frac{XH_y}{\delta})_{i,1}\frac{\Delta x}{2} - 1]p^n_{i+1,1} - [H_{i,1}\frac{4\varepsilon}{\delta\Delta t} - (\frac{XH_y}{\delta})_{i,1}\frac{\Delta x^2}{\Delta y} - 2]p^n_{i,1} \\
&\quad - (\frac{XH_x}{\delta})_{i,1}\frac{\Delta x^2}{\Delta y}p^n_{i,2} + [H_{i,1}\frac{2\varepsilon}{\delta\Delta t} - (\frac{XH_y}{\delta})_{i,1}\frac{\Delta x}{2} - 1]p^n_{i-1,1} \\
D_j &= -(1 + \frac{\Delta x}{2}C_{ij} - \frac{\Delta x}{\Delta t}EE_{ij} - \frac{2}{\Delta t}EG_{ij})p^n_{i+1,j} - (\frac{\Delta x}{4\Delta y}B_{ij} - \frac{\Delta x}{2\Delta y\Delta t}EK_{ij})p^n_{i+1,j+1} \\
&\quad + (\frac{\Delta x}{4\Delta y}B_{ij} - \frac{\Delta x}{2\Delta y\Delta t}EK_{ij})p^n_{i+1,j-1} + 2[1 + (\frac{\Delta x}{\Delta y})^2A_{ij} - \frac{2}{\Delta t}EG_{ij} - \frac{2}{\Delta t}(\frac{\Delta x}{\Delta y})^2EF_{ij}]p^n_{i,j} \\
&\quad - [(\frac{\Delta x}{\Delta y})^2A_{ij} + \frac{\Delta x^2}{2\Delta y}D_{ij} - \frac{2}{\Delta t}(\frac{\Delta x}{\Delta y})^2EF_{ij}]p^n_{i,j+1} - [(\frac{\Delta x}{\Delta y})^2A_{ij} - \frac{\Delta x^2}{2\Delta y}D_{ij} \\
&\quad - \frac{2}{\Delta t}(\frac{\Delta x}{\Delta y})^2EF_{ij}]p^n_{i,j-1} - (1 - \frac{\Delta x}{2}C_{ij} + \frac{\Delta x}{\Delta t}EE_{ij} - \frac{2}{\Delta t}EG_{ij})p^n_{i-1,j} + (\frac{\Delta x}{4\Delta y}B_{ij} \\
&\quad - \frac{\Delta x}{2\Delta y\Delta t}EK_{ij})p^n_{i-1,j+1} - (\frac{\Delta x}{4\Delta y}B_{ij} - \frac{\Delta x}{2\Delta y\Delta t}EK_{ij})p^n_{i-1,j-1} \\
D_M &= FP(i,M)
\end{aligned}
\right\}, \quad (33)
$$

where the offshore index i is identified as the same as that in the coefficient matrices.

For (28), B_b is the identity matrix and A_b is simply the negative of B_b. The column vector D_b is given by:

$$
\left.
\begin{aligned}
D_{b_j} &= (\frac{X\Delta x}{\delta}\tau^y_w)_j \\
D_{b_M} &= FP(1,M)
\end{aligned}
\right\}. \quad (34)
$$

The solution to (27)-(29) is again obtained through the use of a recurrence formula:

$$f_i^{n+1} = \tilde{\alpha}_i \, f_{i-1}^{n+1} + \beta_i, \tag{35}$$

where $\tilde{\alpha}_i$ is a N x N matrix and β_i a N-component column vector. By direct substitution, based upon (35), for f_{i+1}^{n+1} in (27), it follows that

$$\left.\begin{aligned} \tilde{\alpha}_i &= -\,(\tilde{B} + \tilde{C}\,\tilde{\alpha}_{i+1})^{-1}\,\tilde{A} \\ \beta_i &= (\tilde{B} - \tilde{C}\,\tilde{\alpha}_{i+1})^{-1}\,(D - \tilde{C}\,\beta_{i+1}) \end{aligned}\right\}. \tag{36}$$

On the basis of (29),

$$\tilde{\alpha}_N = 0, \quad \beta_N = 0.$$

Consequently, all coefficient matrices and column vectors in the recurrence formula are determined.

Upon using (35), it follows from (28) that

$$f_1^{n+1} = (\tilde{A}_b + \tilde{B}_b\,\tilde{\alpha}_2)^{-1}\,(D_b - \tilde{B}_b\,\beta_2). \tag{37}$$

The recurrence relation (35) then completes the specification of all f_i^{n+1}, thus the pressure field at time step n+1 over the entire HSV region.

Once the pressure is known, the inviscid velocity components to the zeroth order are calcualted from the geostrophic balance which, in the transformed coordinates reads nondimensionally:

$$\left.\begin{aligned} v &= \frac{1}{X}\, p_x \\ u &= -\, p_y - F p_x \end{aligned}\right\}, \qquad (38)$$

where

$$F = -\,(xX' + X_1')/X.$$

The velocity field calcuated from (38) is then compared to direct current measurements made above the bottom boundary layer in the HSV region.

4. Hindcast

The numerical models developed above are used to hindcast currents above the bottom boundary layer in the New York Bight from 7 March to 30 April of 1975. The model is driven in part by wind stresses derived from six-hourly winds observed at the John F. Kennedy airport. The derivation of the kinematic wind stress components is in accordance with the following bulk aerodynamic formula:

$$(\tau_w^x, \tau_w^y) = 0.02\ (0.515)^2\ W\ (W^x, W^y), \qquad (39)$$

where W(kt) is the wind speed, and (W^x, W^y) (kt) are wind components in the (x,y) directions, respectively. (The coordinate directions in the CSW-region are used in data presentation throughout this Section).

The above formula implies a drag coefficient, C_D, of 1.6×10^{-3} for the dynamic stress with wind speed and components in cm sec^{-1}. Fig. 2 presents time series plots of the derived x-directed (onshore) and y-directed (alongshore) wind stress components from 6 March (Julian Day 65) to 30 April (Julian Day 120) of 1975. The passage of winter storms is easily identified by major bursts of offshore wind-stresses directed to the southeast. The fluctuations in the alongshore wind-stress component is weaker in comparison. Two relatively large perturbations to the southwest (negative y-direction) occur apparently as part of the storms that gave rise to strong offshore (negative x-directed) stresses on 4 and 20 April (Julian Day 94 and 110, respectively).

The other part of the model forcing comes from alongshore flows measured

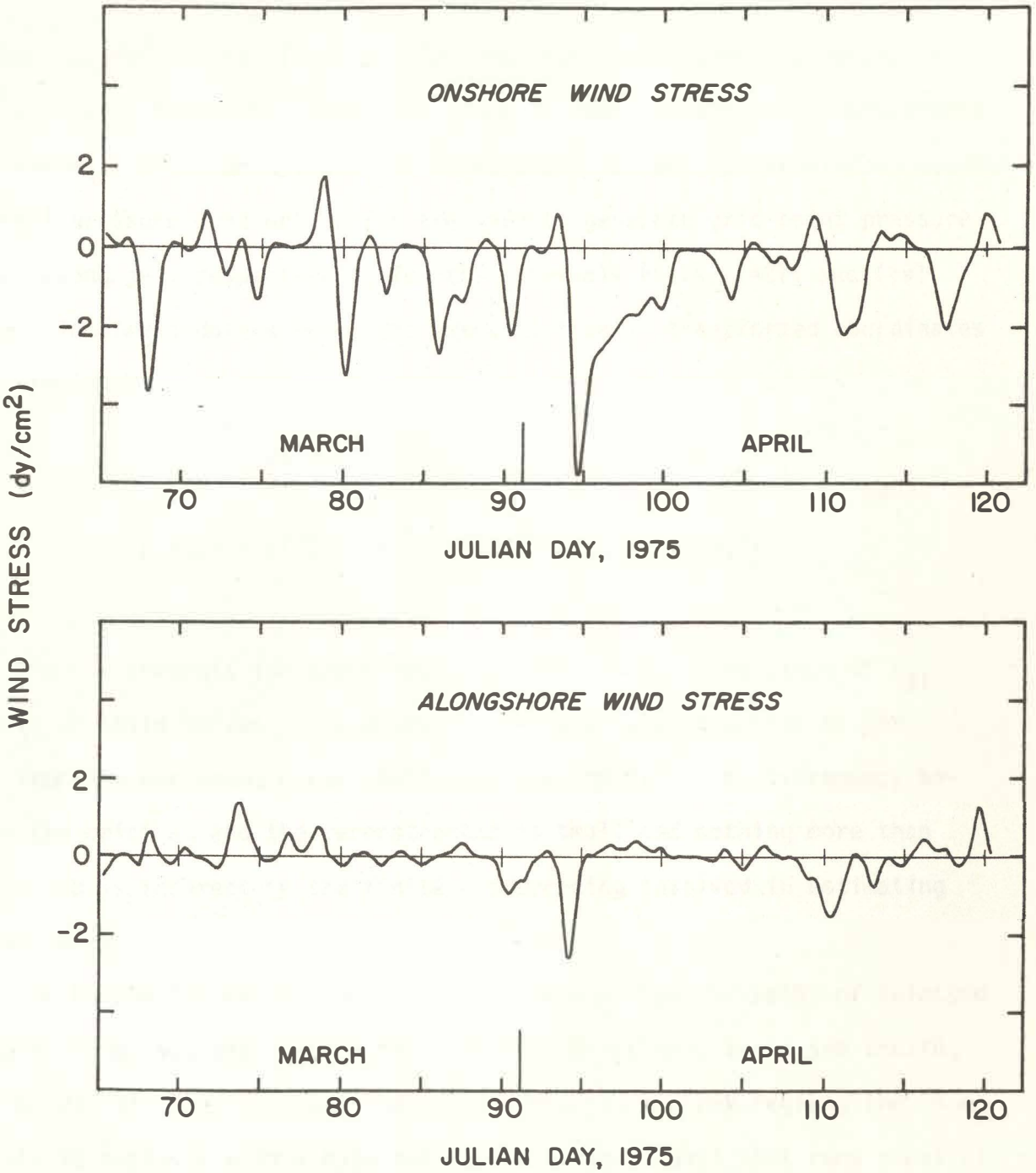

Fig. 2. Time series plots of (a) onshore and (b) alongshore wind stresses for the period of 6 March - 30 April, 1975. The stresses are computed from six-hourly observed winds at the John F. Kennedy airport according to : $(\tau_w^y, \tau_w^y) = 0.02\ (0.515)^2\ W\ (W^x, W^y)$, where W (kt) is the wind speed and (W^x, W^y) (kt) are, respectively, wind components in the onshore (northwest) and alongshore (southwest) directions.

at Stations P31 and P32 (i=17 and 10, respectively, in the CSW convention) (see Fig. 1). Since the alongshore flows are geostrophic, the y-components (v_{31} and v_{32}) of velocity measured at Stations P31 and P32 provide an estimate of local pressure gradients which are used to generate grid-point pressure values along j=1, respectively, for the intervals (i=14, i=21) and (i=1, i=13). In dimensionless form, the extrapolation in transformed coordinates is as follows:

$$p(i,1) = (i-1)\ X(1)\ v_{32}\ \Delta x,\ i=1,\ 13$$
$$p(i,1) = p(13,1) + (i-13)X(1)\ v_{31}\ \Delta x,\ i=13,21 \qquad (40)$$

Fig. 3 presents for the hindcast period, time series plots of v_{31} and v_{32} in solid curves. The dashed curves are reconstruction of the same from the upstream, cross-shelf pressure inputs. The discrepancy between the original and the reconstructed is small and nothing more than that which is inherent in the finite differencing involved in estimating v from $\Delta p/\Delta x$.

The bathymetry of the models is constructed from the paths of selected isobaths from C&GS chart No. 1108. In the CSW-regions, these are the 18, 37, 55, 73, 91, 110, 137, and 183 m isobaths. In the HSV-region, the 18 m isobath is replaced with a hypothetical zero-depth coast that runs parallel to the y-axis through a point 20 km offshore (in the x-direction) from the John F. Kennedy airport. Water depths at grid points along each transect (fixed j) are interpolated from the depths at the key isobath positions. Fig. 4 shows a computer-contoured presentation of the model bathymetry. The Hudson Shelf

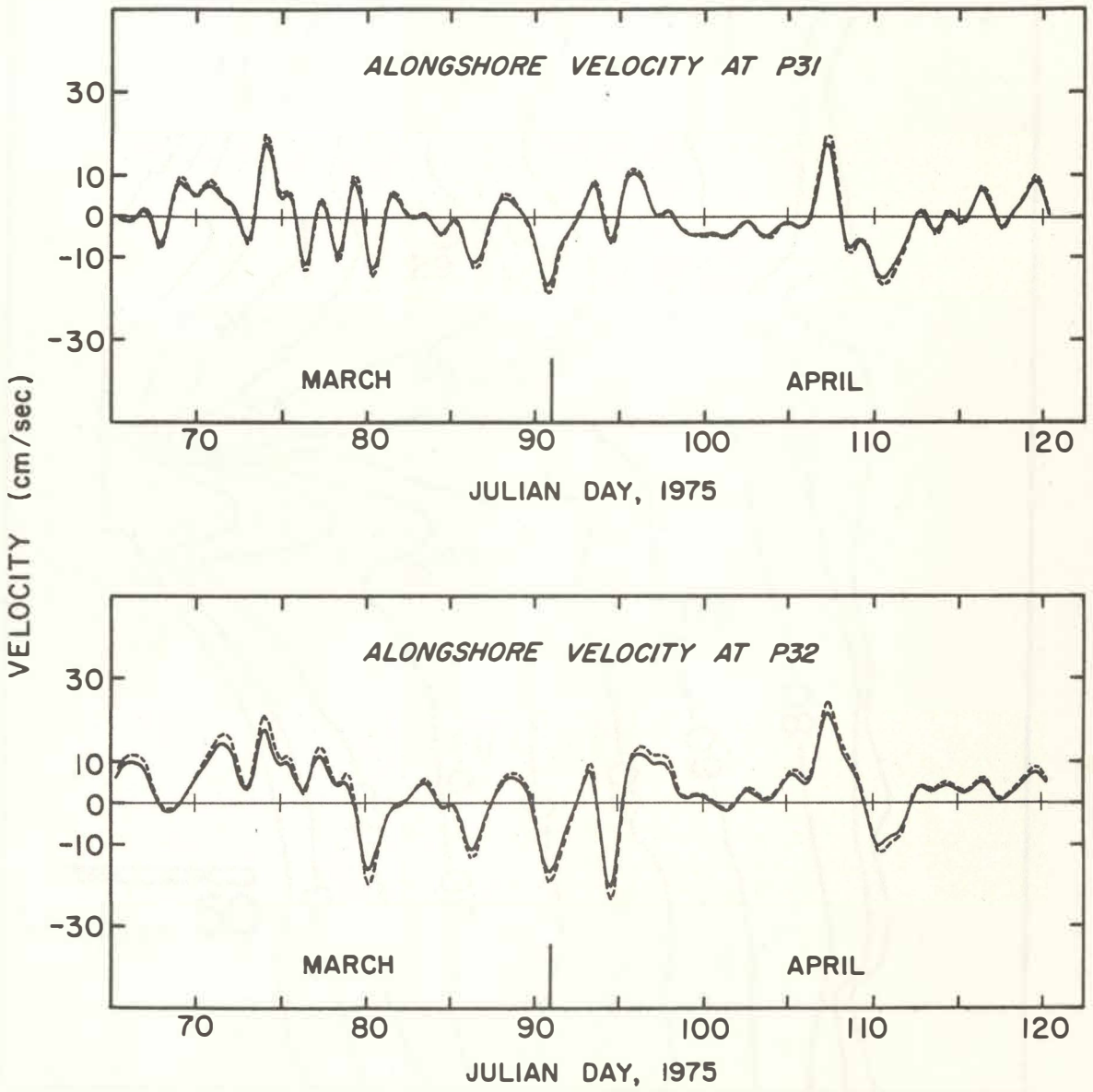

Fig. 3. Time series plots of alongshore (southwestward) current velocities at (a) P31 and (b) P32 for the period of 6 March - 30 April, 1975. The solid curves represent low-pass-filtered velocity measurements decimated at six-hour intervals. The filter allows half-power passage at 40 hr. periodicity. The dashed curves are reconstructions from cross-shelf pressure distributions used to drive the model.

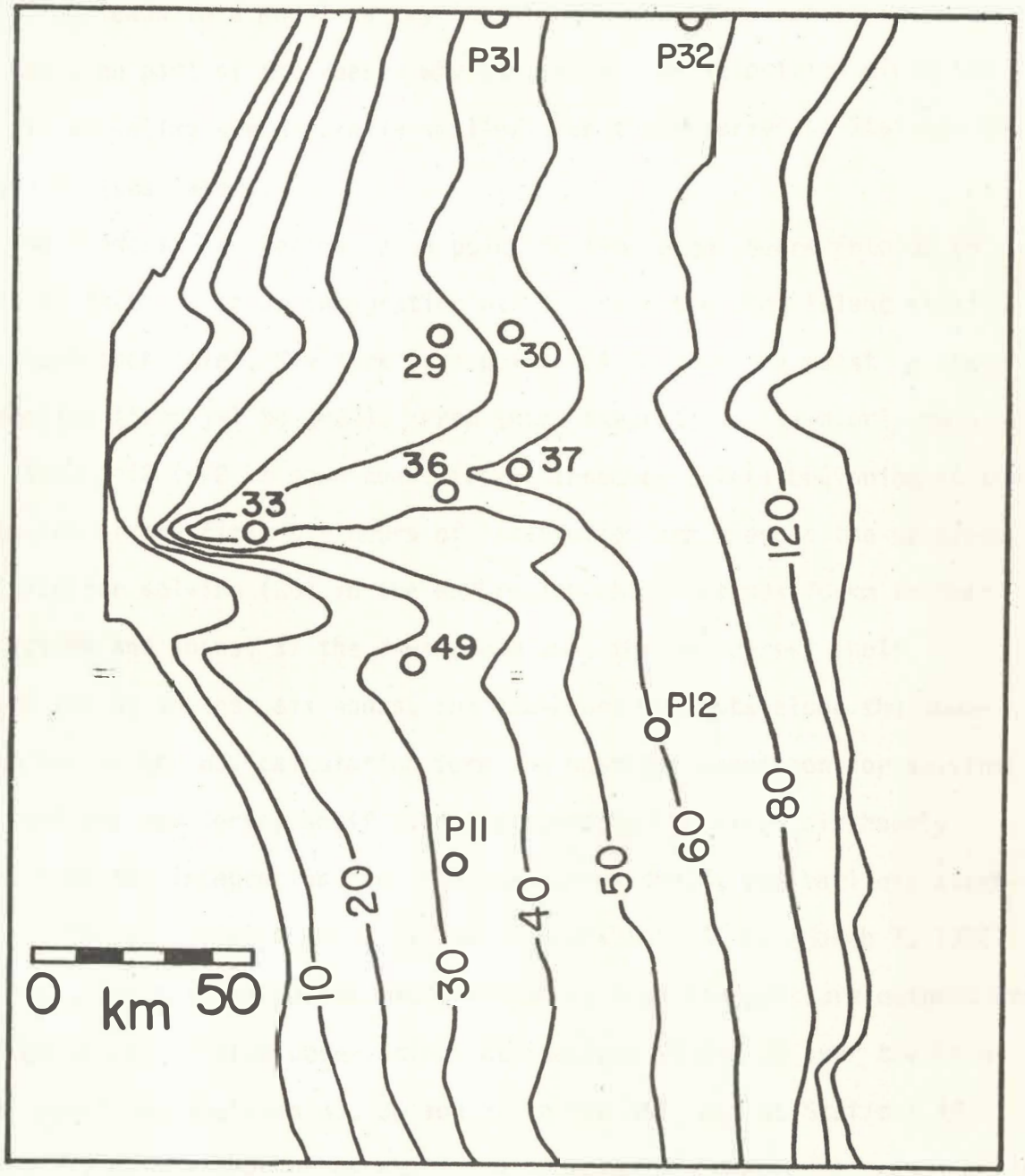

Fig. 4. The model bathymetry of the New York Bight. Except for the Hudson Shelf Valley region, a coastal wall is placed along the 10 m isobath. The coastline is at zero depth and the offshore-most contour is at 180 m. Current meter mooring stations are shown where comparisons are made between model velocity outputs and observed currents.

Valley formation is reasonably well represented, although the limited y-resolution leads to a model valley that is much broader than is in reality. This could be part of the reason why the calculated velocities along the axis of the valley are generally smaller than the observed at Stations 33, 36, and 37 (see later).

The hindcast run begins, at a point in time eight hours into JD 65 (March 6, 1975), with an integration of (10) over the Long Island shelf from Shennecock Inlet, New York to a point 124 km down the coast in the y-direction (from j=1 to j=20). From this integration, six-hourly outputs along j=12 (~72 km down-coast from Shinnecock Inlet) beginning at the conclusion of the first six hours of integration are used as the upstream condition for solving (20) in the HSV region which extends 70 km in the y-direction and joins, at the downstream end, the New Jersey shelf. Delayed yet by another six hours, the six-hourly outputs along the downstream end of the HSV calculation form the upstream condition for solving (10) over the New Jersey shelf. Upon discarding the first six-hourly output from the integration over the New Jersey shelf, the earliest starting time for all model outputs is thus 2 hours into JD 66 (March 7, 1982).

The velocities calculated at grid points from the pressure outputs are compared to near-bottom observations at Stations 29 and 30 over the Long Island shelf, at Stations 33, 36 and 37 in the HSV, and at Stations 49, P12 and P11 on the New Jersey shelf. At station 49, the model velocity time series may be generated from either the HSV output or the New Jersey shelf output. Since the resulting velocity time series are very similar, the one generated with the HSV output is used in further discussion. Fig. 5 presents

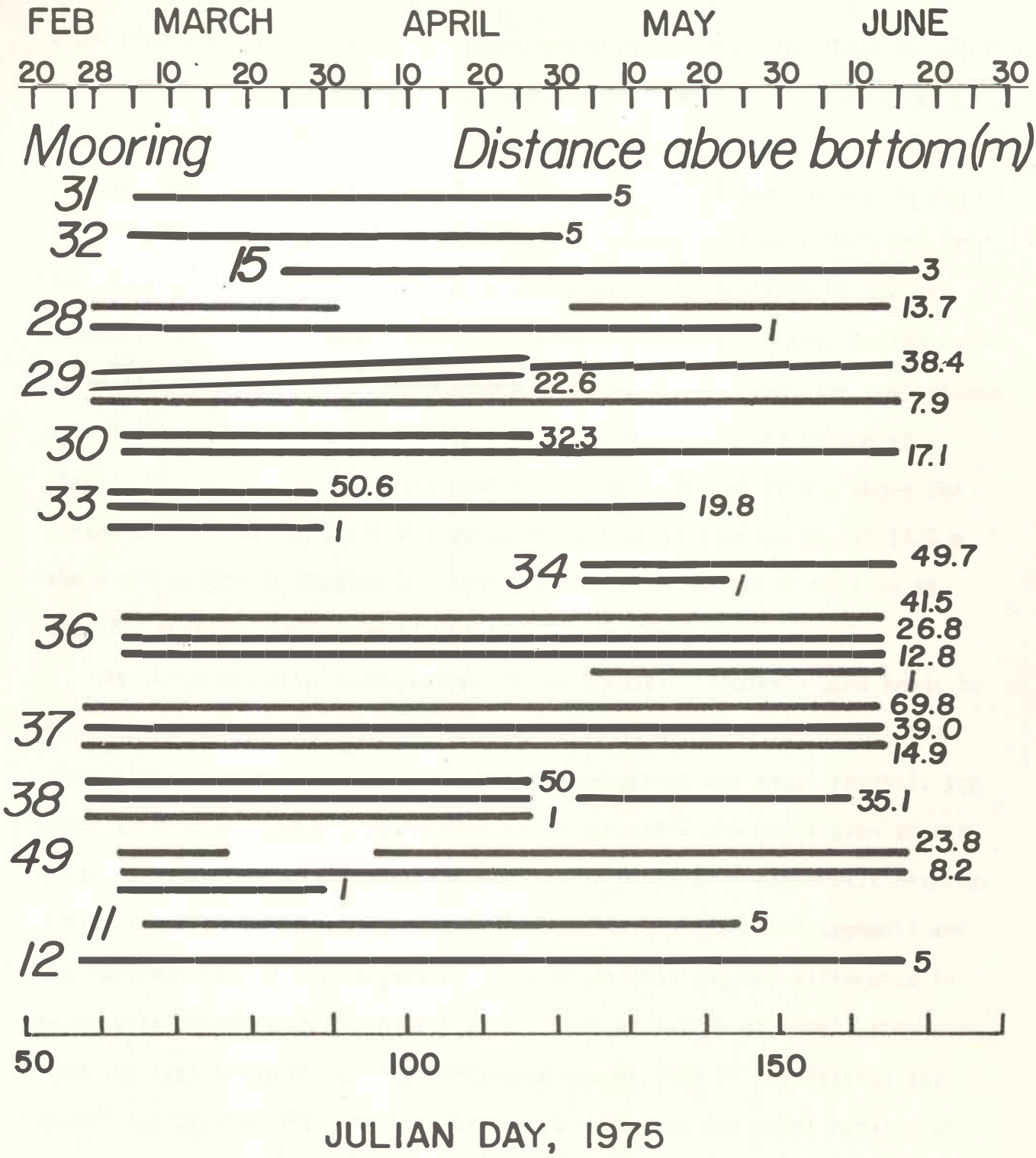

Fig. 5. A bar chart of available current meter data from the AGOB experiment in 1975.

a bar chart of available current meter measurements that were made during the 1975 AGOB experiment. Comparisons between model results and direct velocity observations are presented only for locations where there is no interruption in data time series. Consequently, Stations 15 and 28 that appear in Fig. 1 are excluded. To avoid the contamination of near surface noises and the influence of the surface Ekman layer whose vertical structure is not resolved in the model, comparisons are further restricted to near bottom currents that are outside of the bottom frictional layer. Thus the comparisons only involve observed current velocities at 7.9 m above the bottom at Station 29, at 17.1 m above the bottom at Station 30, at 19.8 m above the bottom at Station 33, at 12.8 m above the bottom at Station 36, at 14.9 m above the bottom at Station 37, at 8.2 m above the bottom at Station 49, and at 5 m above the bottom at Stations P11 and P12.

As large velocity fluctuations in the synoptic frequency band tends to occur along the local tangent to depth contours, to bring into focus the similarities and differences between the observation and model results, the velocity fluctuations are decomposed along the major and minor axes at each location where the comparision is made. Fig. 6 presents major axis orientations at mooring stations for model fluctuations (dashed line segment) and the observed (solid line segment). At a given station, the difference in major axis orientation is chiefly a result of deviation of model bathymetry from the real bathymetry. The difference ranges from 9^{o} (at Station 30) to 44^{o} (at Station 49). No orientation is indicated for model results at Stations P31 and P32 since no comparison is made at these stations where the observed fluctuations in alongshore flow are incorporated as part of model forcing. The minor axis at any given station is of course given simply

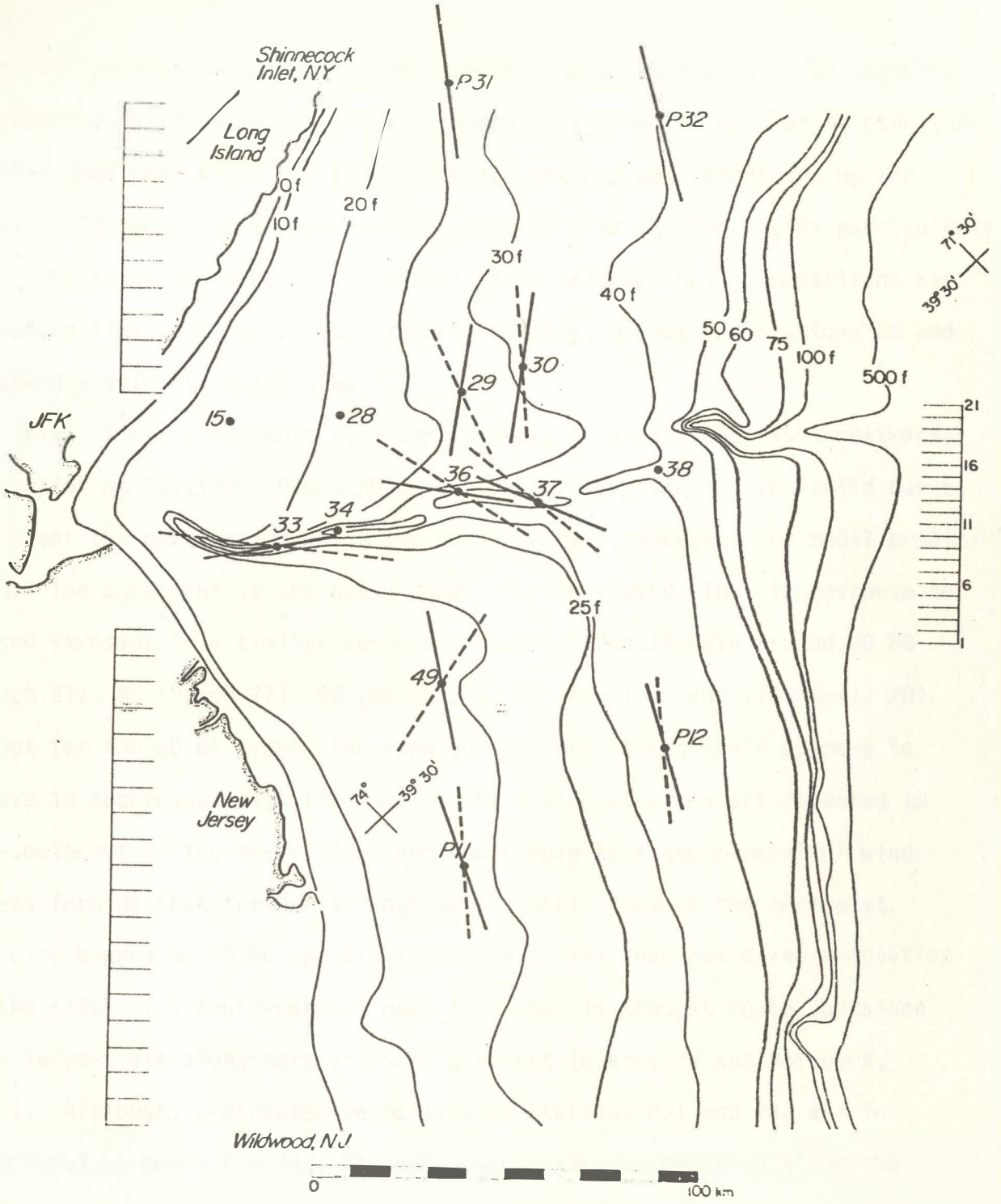

Fig. 6. Major axis orientations for velocity fluctuations at current meter mooring stations where comparisons are made between model results and observations. The solid (dashed) lines indicate orientations along which most of the observed (model) fluctuating velocities are aligned for the period of 7 March - 30 April, 1975.

by a line perpendicular to the line segments shown in Fig. 6. The velocity fluctuations along a minor axis are, however, typically an order of magnitude smaller than that along the major axis and are not well-predicted by the model. (The model upstream condition derived from v_{31} and v_{32} is particularly deficient as it contains no cross-shelf flow information.) Comparisons are therefore limited to major axis velocities only, except for Stations 29 and 30 where y-velocities are used.

Figs. 7 and 8 presents time series plots of y-directed (southwestward) velocities at Stations 29 and 30 on the Long Island shelf. The solid curves represent the observation while the dashed curves represent the model prediction. The agreement is obviously good. Northeastward flows in response to y-wind stresses in a similar sense are clearly identifiable around JD 80 (March 21), 86 (March 27), 90 (March 31), 94 (April 4) and 110 (April 20). Except for the JD 86 event, the flow on the Long Island shelf appears to behave in accordance with the model. The x-wind stresses are directed to the southeast during these times and contribute to a shore-parallel wind stress forcing that further strengthen the shelf flow to the northeast. The discrepancy on JD 86 appears to be due to the inadequate representation in the model of a southwestward mean flow that is thought to be sustained by a large-scale alongshore pressure gradient (Beardsley and Boicourt, 1981). Although, y-directed velocities at Stations P31 and P32 are incorporated as model forcing, the adiabetic pressure condition along the shelf break effectively shields the model shelf from oceanic alongshore pressure gradients that could contribute to an additional mean flow component to the southwest. This model shortcoming could also explain why

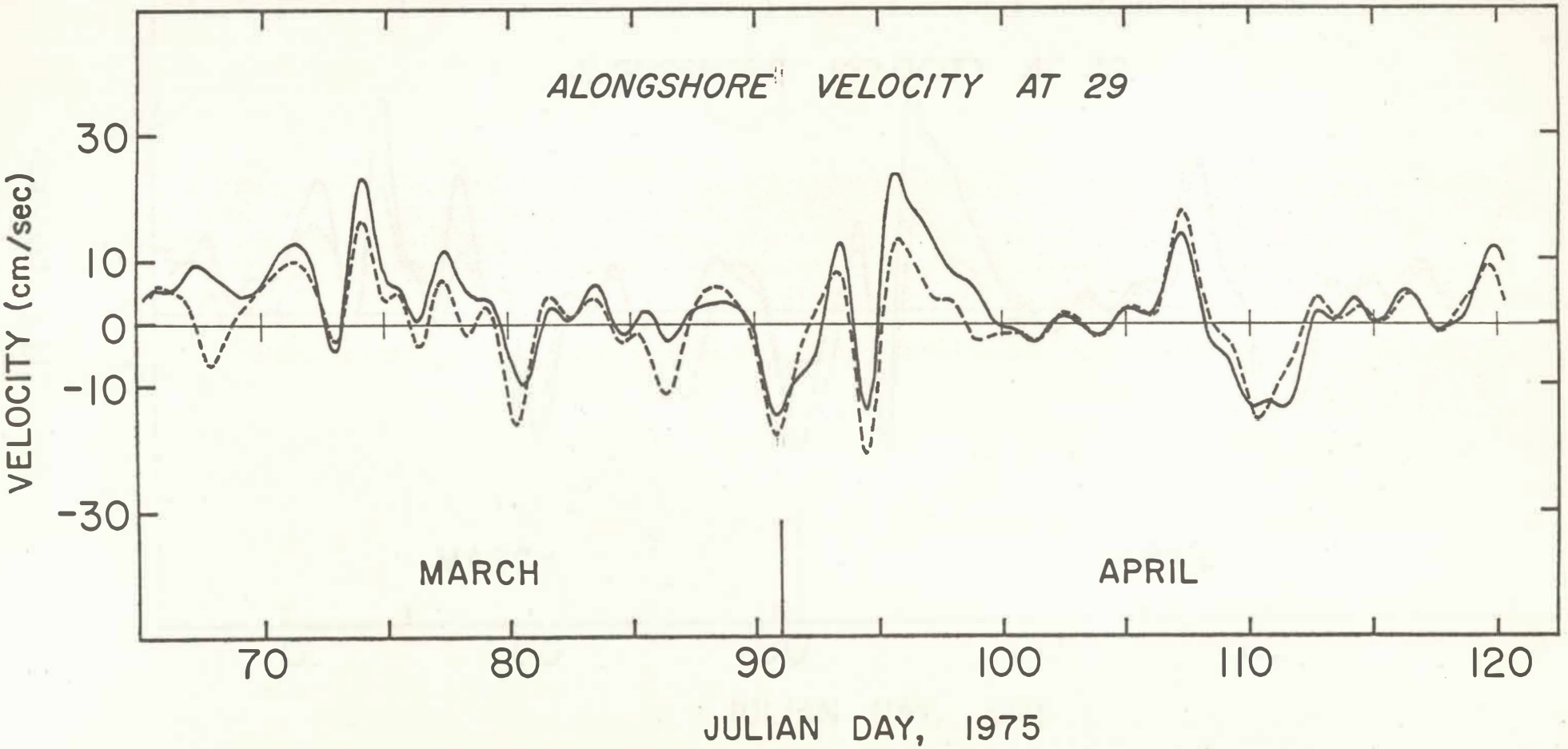

Fig. 7. Time series plots of southwestward velocities at mooring station 29 on the Long Island shelf for the period of 7 March - 30 April, 1975. The solid curve represents the 40-hour low-pass-filtered observations and the dashed curve the model results.

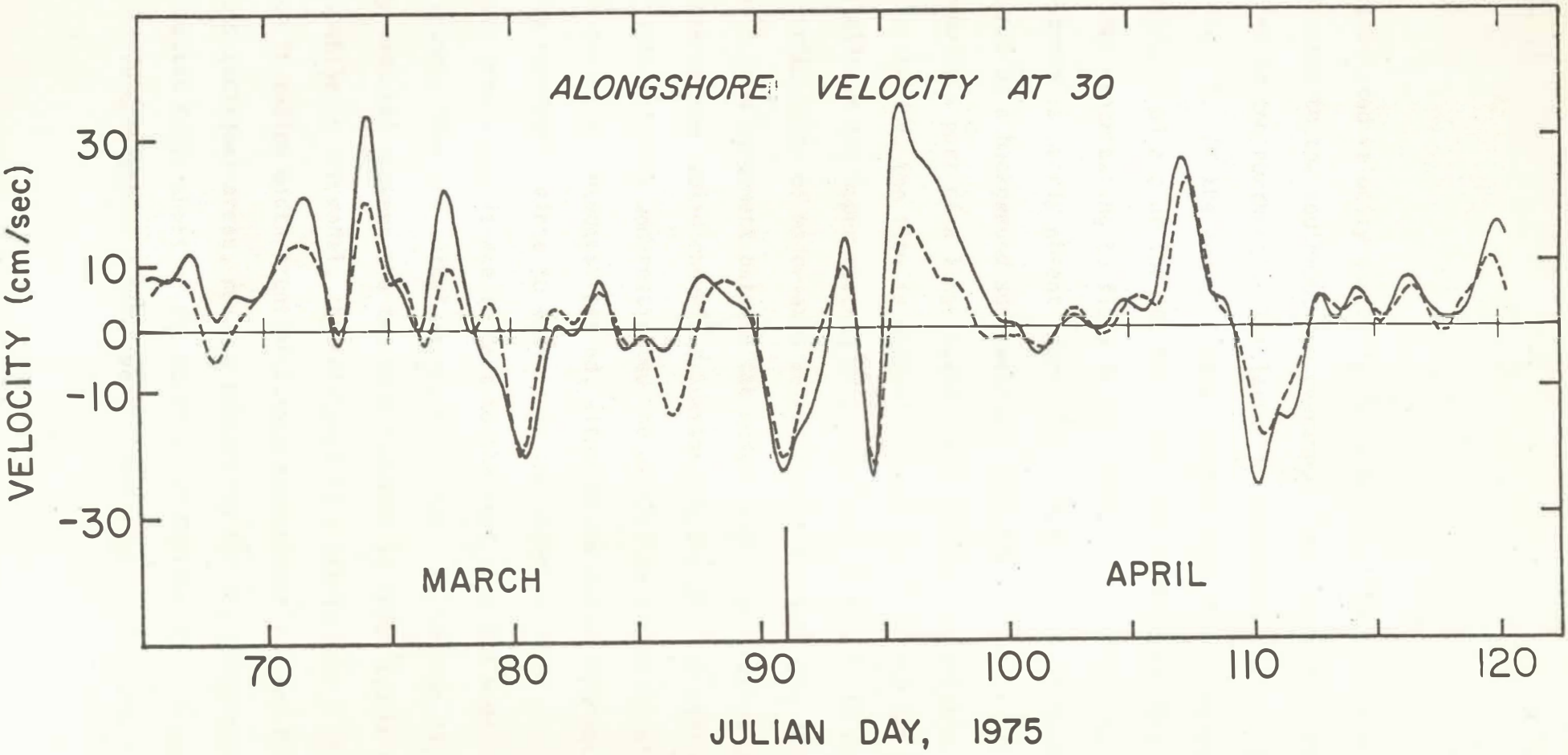

Fig. 8. Time series plots of southwestward velocities at mooring station 30 on the Long Island shelf for the period of 7 March - 30 April, 1975. The solid curve represents the 40-hour low-pass-filtered observations and the dashed curve the model results.

the calculated velocity generally falls short of the observed when the flow is directed to the southwest and overshoots that observed when the flow is directed to the northeast. The latter is particularly so at Station 29 (see Fig. 7). Of the events with a southwestward flow, the ones around JD 96 (April 6) and JD 107 (April 17) are noteworthy, for the wind-stress is either contributing to flows in the opposite direction (April 6) or the wind-stress is nearly absent (April 17). These are clear evidences of the existence of a background southwestward flow that is not locally wind-driven and remains a part of a large scale shelf circulation pattern.

In the HSV, the flow is primarily cross-shelf, along the valley axis, especially in the upper reaches of the valley. Figs. 9, 10 and 11 present time series plots of major-axis velocities at Stations 33, 36 and 37. There is good agreement between the model prediction (dashed curve) and the observation (solid curve) at Stations 36 and 37. At Station 33, the model substantially underestimates the axial flow in nearly all major events during the hindcast period, although the phase information content appears reasonably close to what is in the observed. The shortfall in the velocity prediction is due in part to the fact that the model valley is much broader than the actual valley formation. At Station 33, the cross-valley distance between the two 50 m isobaths is about 2.5 km on the CG&S chart, while in the model, this distance is a little over 5 km. This difference in valley width translates into approximately a two-to-one difference in cross-sectional areas, readily accounting for the proportion by which the computed falls short of the observed at Station 33. In correspondence to the five northeastward flow events identified on the Long Island shelf,

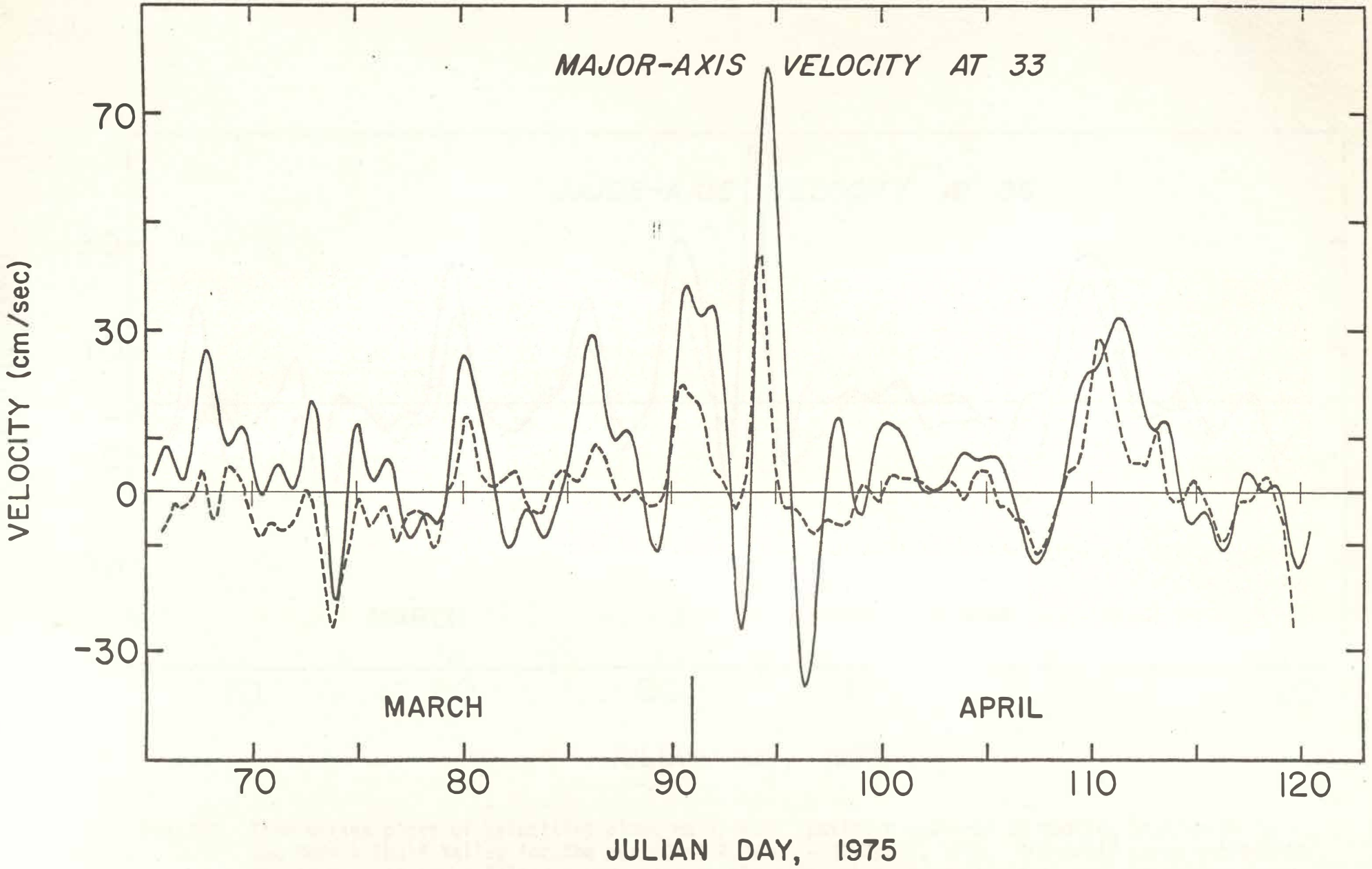

Fig. 9. Time series plots of velocities along major axes (positive onshore) at mooring station 33 in the Hudson Shelf Valley for the period of 7 March - 30 April, 1975. The solid curve represents the 40-hour low-pass-filtered observations along the observed major axis, and the dashed curve model results along the model major axis. See Fig. 6 for the major axis orientations.

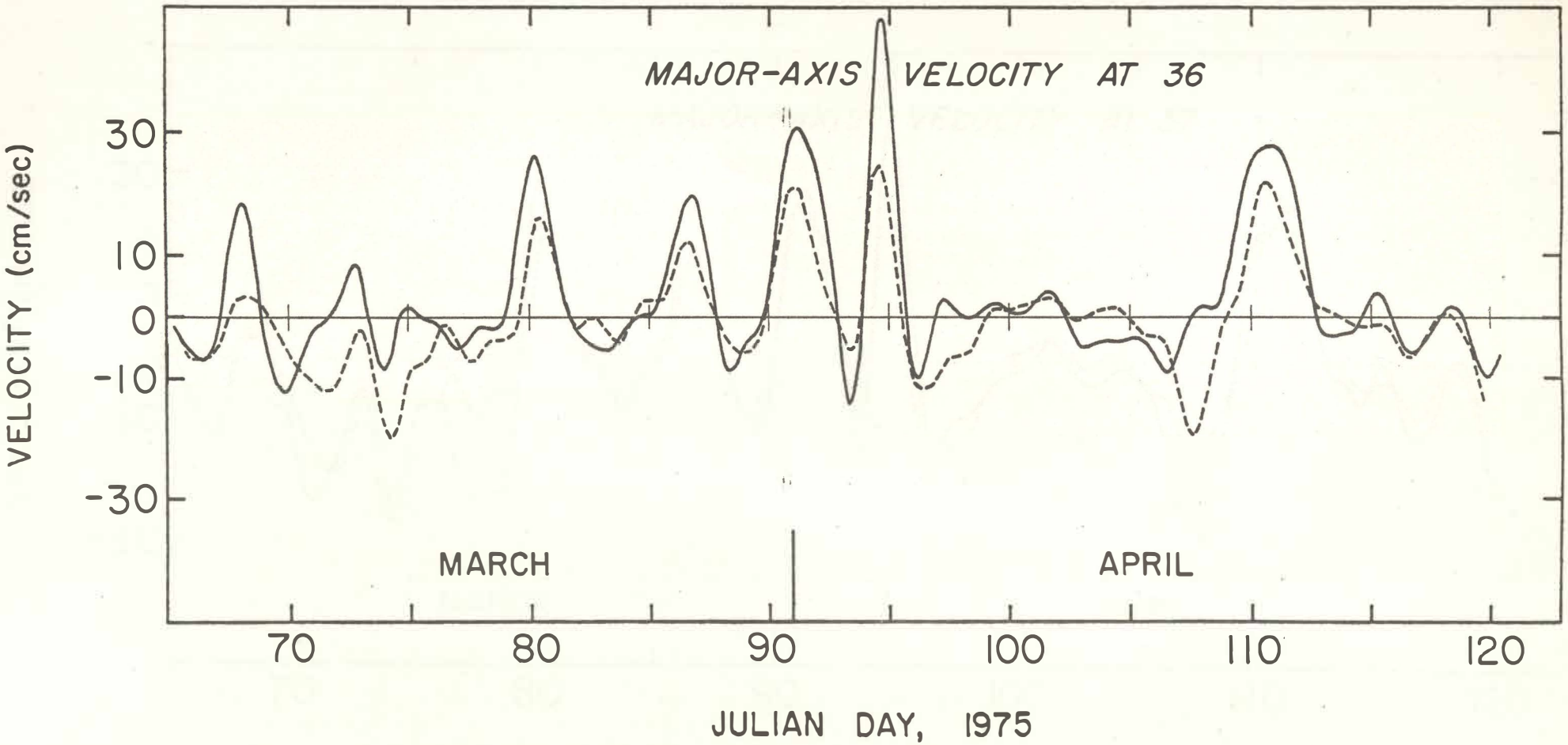

Fig. 10. Time series plots of velocities along major axes (positive onshore) at mooring station 36 in the Hudson Shelf Valley for the period of 7 March - 30 April, 1975. The solid curve represents the 40-hour low-pass-filtered observations along the observed major axis, and the dashed curve represents model results along the model major axis. See Fig. 6 for the major axis orientations.

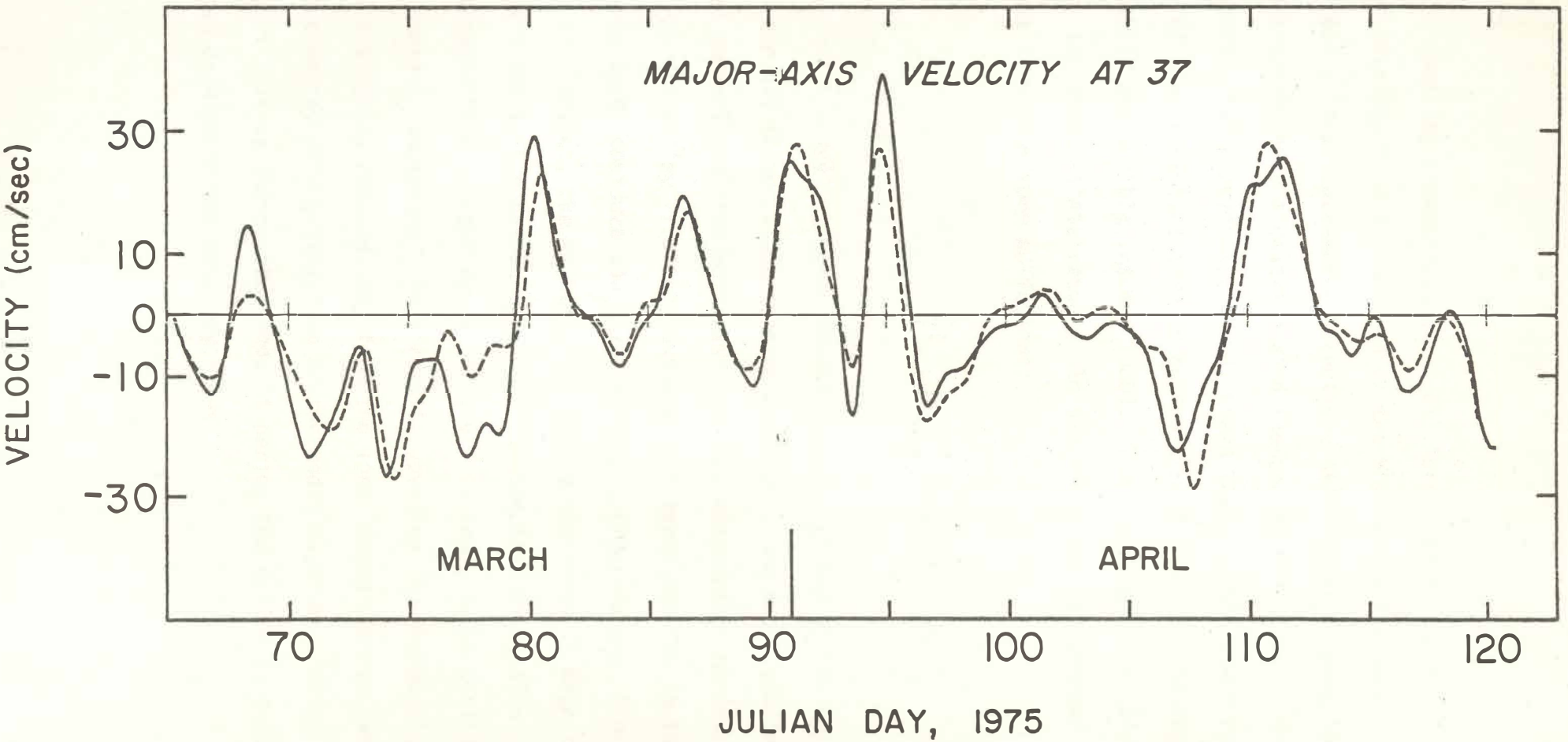

Fig. 11. Time series plots of velocities along major axes (positive onshore) at mooring station 37 in the Hudson Shelf Valley for the period of 7 March - 30 April, 1975. The solid curve represents the 40-hour low-pass-filtered observations along the observed major axis and the dashed curve represents model results along the model major axis. See Fig. 6 for the major axis orientations.

bursts of upvalley flow are found at all three valley stations. The occurrence of upvalley flow at the head of the HSV, where the valley axis turns to run nearly in a south-north direction, has been attributed to the onshore Ekman transport under a eastward wind (Nelsen et al., 1978). In the steady-state study cited previously, it was shown that, in the lower reaches, the turning of the streamline induced by the curved paths of the depth contours is primarily responsible (Hsueh, 1980). The time-dependent calculation confirms the steady-state result. To see this, the homogeneous form of (6) is recast in vector form as follows:

$$\vec{v}^I \cdot \nabla H = w_E + Hf^{-1} \hat{k} \cdot \nabla x \vec{v}^I_t, \qquad (41)$$

where $w_E = \delta \hat{k} \cdot \nabla x \vec{v}^I$ is the vertical velocity at top of the bottom Ekman layer. For all three valley station locations, the depth gradient vector is directed generally to the northeast. As the wind-driven northeastward flow approaches the valley from the southwest, it turns onshore to follow the underlying depth contours and gives rise to a negative u_y. Since the shelf flow is wind-driven, the negative y-velocity increases in magnitude onshore, and this leads to a negative v_x. Thus, in the five cases of wind-driven northeastward flow, according to (41), $\vec{v} \cdot \nabla H$ tends to be positive in the valley where u_y dominates. As a result, upvalley flow takes place in a direction slightly rotated away from the local depth contour tangent in a clockwise sense. The orientation of the model major axis (Fig. 6) appears to support this as during the hindcast period the valley circulation is dominated by wind-driven upvalley flows.

The two southwestward flow events identified on the Long Island shelf that are not locally wind-driven also leave impressions on the flow in the HSV. Both the model result and observation indicate a downvalley flow in response to these events on the shelf (see Figs. 9-11). This can again be explained by (41). For, in the case, v_x 0 and u_y 0 on the southwestern bank of the valley, and v · H is negative, leading to a flow directed more than 90^o clockwise from the depth gradient vector which is pointed in a generally northeast direction. (That v indeed increases offshore during these events can be seen clearly in Figs. 3, 7 and 8). It is thus clear that the steady-state mechanism for the axial flow in the valley remains valid for the time-dependent flow. In the time-dependent problem, there is of course the additional mechanism associated with the change of vorticity with time that contributes to the flow orientation. To examine the extent to which this new mechanism is important to the valley flow, model axial velocities at Stations 33, 36 and 37 are averaged over JD 89-91 (March 30 to April 1), a period over which mean conditions are used to calculate the mean flow in the steady state study (Hsueh, 1980). The difference between the mean of the time-dependent calculation and the steady-state results in within 10% at Stations 33 and 37, and about 30% at Station 36. The small discrepancy between the two underscores the fact that over the duration of an individual event, the net contribution of the time-dependent term is small. Thus a steady-state representation of the event-average appears to be no worse than that which is contained in a time-dependent calculation.

The good agreement between predicition and observation persists at station 49, P11 and P12 on the New Jersey shelf (Figs. 12-14). It is of interest

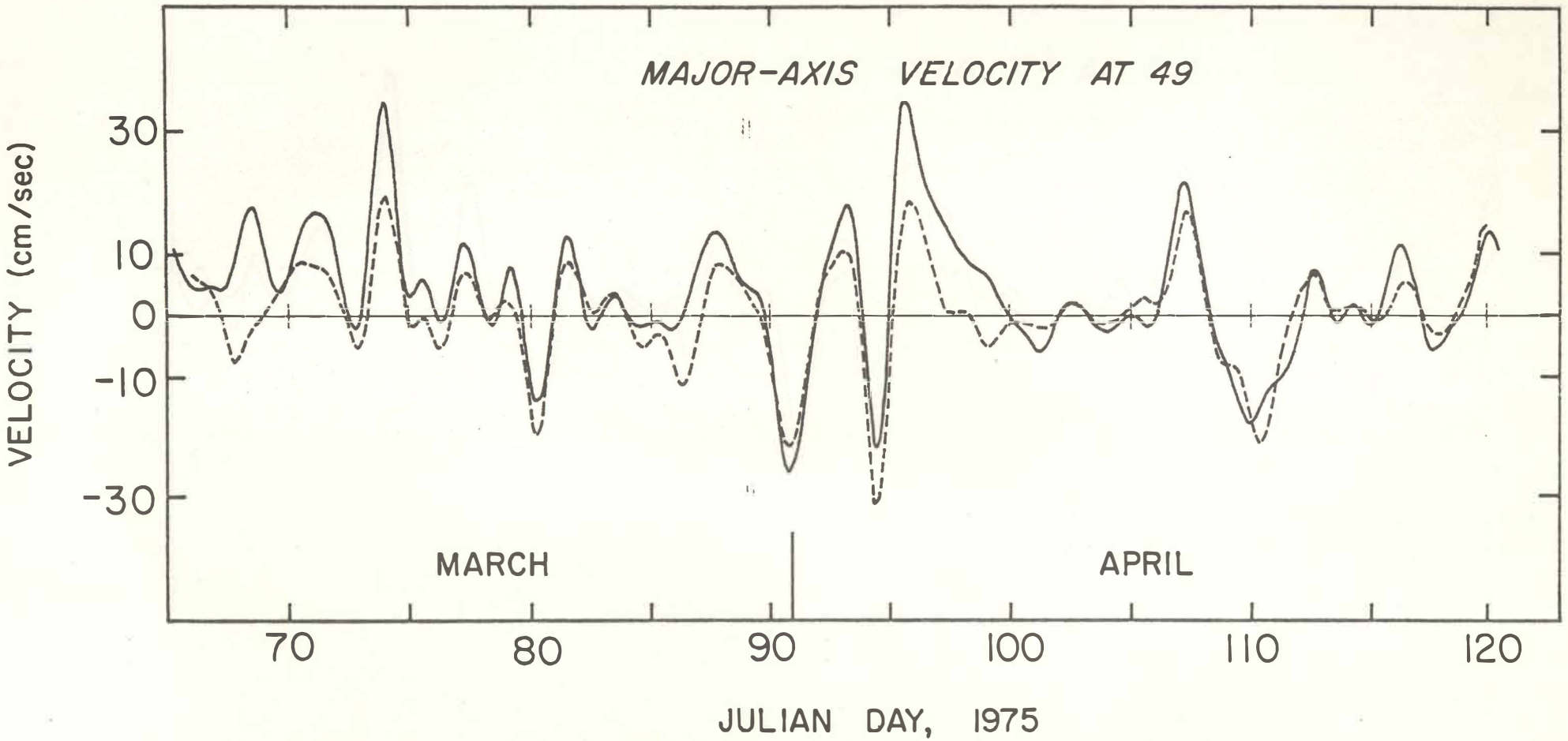

Fig. 12. Time series plots of velocities along major axes (positive to the southwest) at mooring station 49 on the New Jersey shelf for the period of 7 March - 30 April, 1975. The solid curve respresents the 40-hour low-pass-filtered observations along the observed major axis and the dashed curve represents the model results along the model major axis. See Fig. 6 for the major axis orientations.

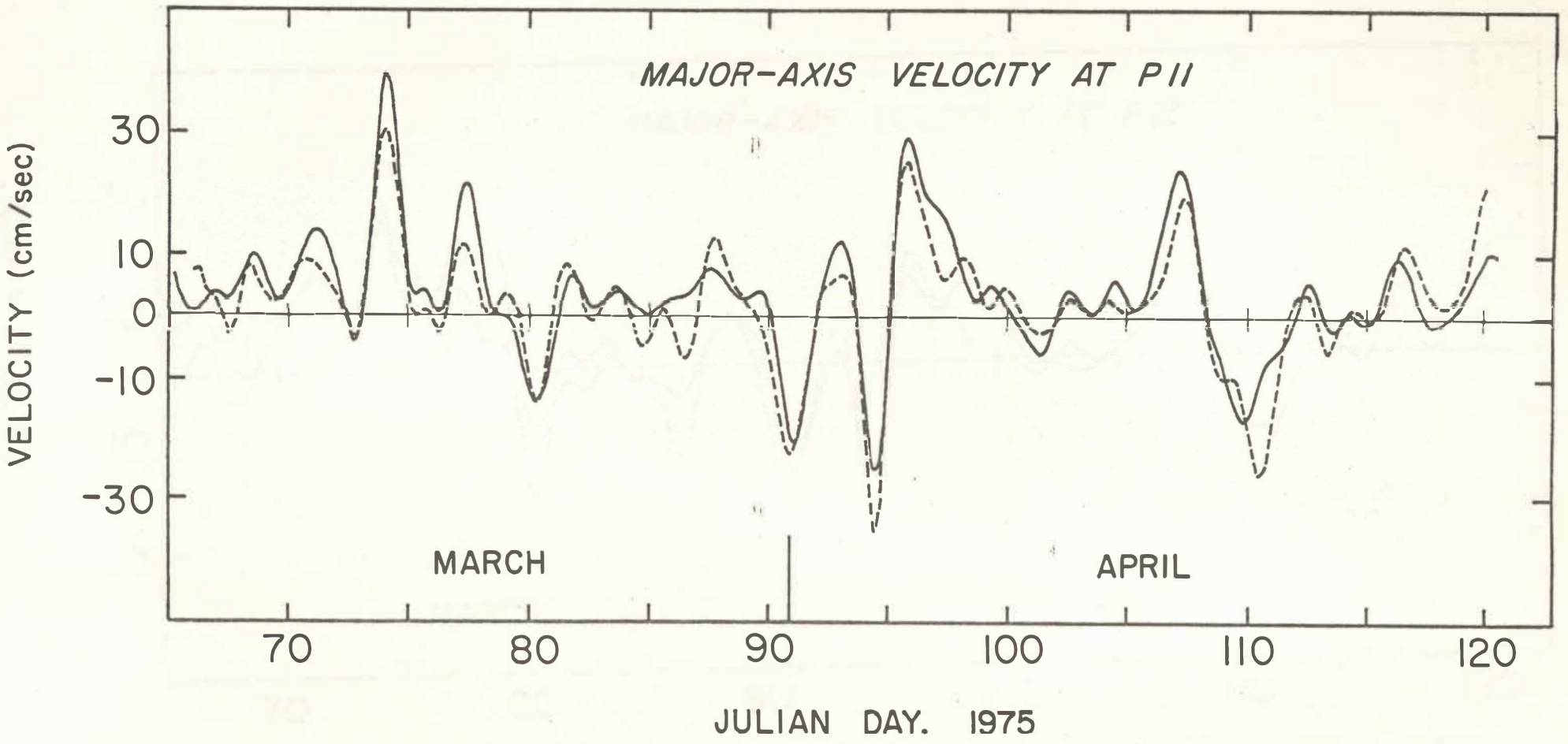

Fig. 13. Time series plots of velocities along major axes (positive to the southwest) at mooring station P11 on the New Jersey shelf for the period of 7 March - 30 April, 1975. The solid curve represents the 40-hour low-pass-filtered observations along the observed major axis and the dashed curve represents model results along the model major axis. See Fig. 6 for the major axis orientations.

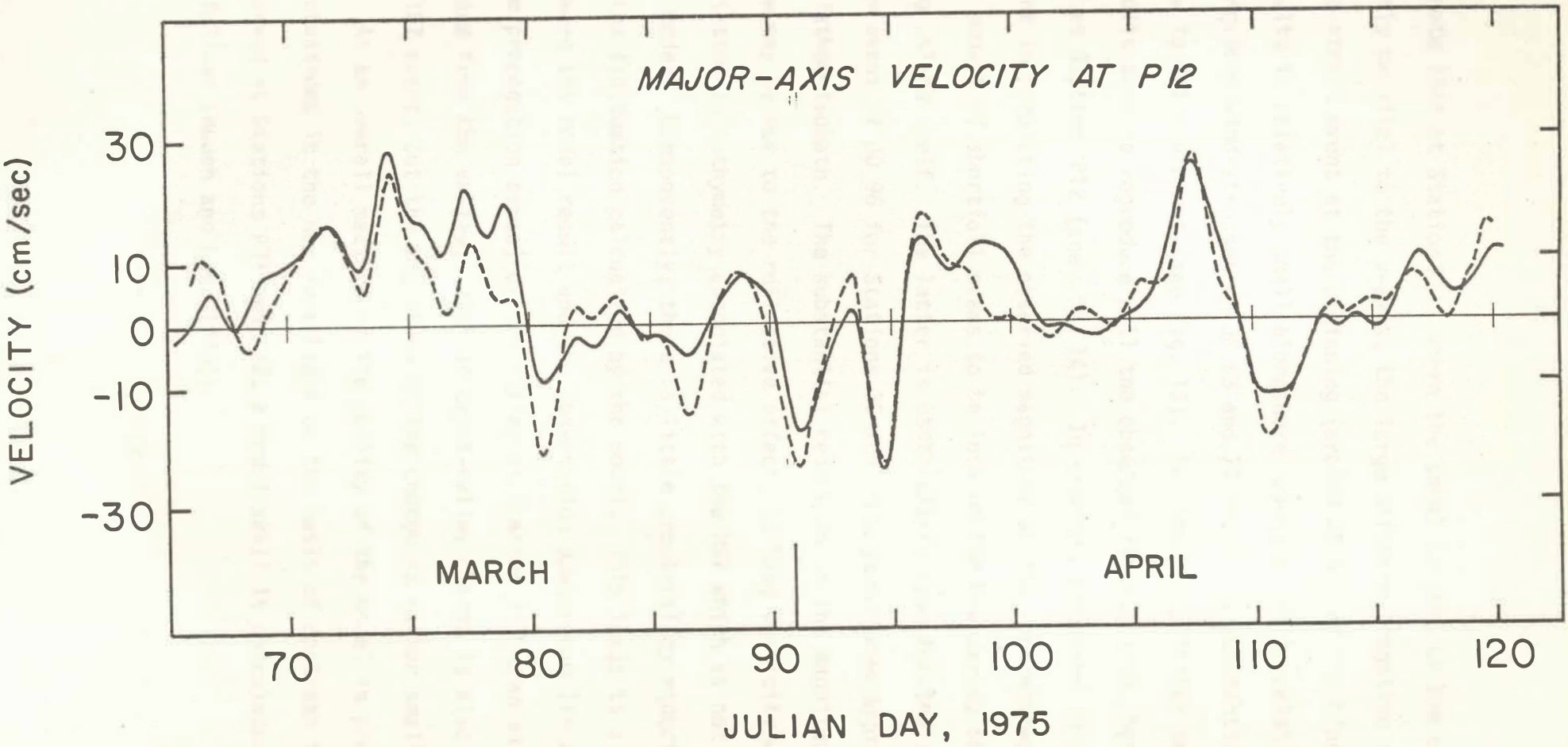

Fig. 14. Time series plots of velocities along major axes (positive to the southwest) at mooring station P12 on the New Jersey shelf for the period of 7 March - 30 April, 1975. The solid curve represents the 40-hour low-pass-filtered observations along the observed major axis and the dashed curve represents model results along the model major axis. See Fig. 6 for the major axis orientations.

to note that at Station P11, where the local tangent to the coastline is nearly parallel to the y-axis, the large offshore (negative x-directed) wind-stress event at the beginning (around JD 67) of the hindcast period results in relatively small alongshore velocity, while relatively small alongshore wind-stresses on JD 68 and 70 result in substantial amount of flow to the southwest (see Fig. 13). For these two latter events, the model results seem to reproduce well the observed fluctuations, here at Station P11 and at Station P12 (see Fig. 14). In general, the model results still falls short in predicting the observed magnitude of the southwestward flow, although the amount of shortfall seems to be less on the New Jersey shelf than on the Long Island shelf. The latter is particularly true for the southwestward flow event of JD 96 for Stations 30 and P12, positioned approximately along the 30-fathom isobath. The substantial reduction in the magnitude of the observed flow may be due to the reflective effect, on long vorticity waves, of the sharp variation in bathymetry associated with the HSV which is not well-resolved in the model. Consequently, there is little cross-valley reduction in amplitude of the fluctuation calcualted by the model. This leads to a better agreement between the model result and the observation downstream (in the long vorticity wave propagation sense) of the valley at Station P12 than at Station 30, upstream from the valley. Similar cross-valley change is also present for the JD 107 event, but the magnitude of the change is rather small.

As an overall measure of the ability of the model in predicting current fluctuations in the New York Bight on the basis of upstream flow conditions observed at Stations P31 and P32, a model skill is calculated that is defined as follows (Hsueh and Lee, 1978):

$$\text{Model Skill} = \frac{\{\int (v_2' - v_1')^2_{obs}\, dt - \int (v'_{2_{obs}} - v'_{2_{comp}})^2 dt\}}{\int (v_2' - v_1')^2_{obs}\, dt} \cdot 100, \qquad (42)$$

where the prime indicates demeaned fluctuations, the subscript "1" indicates the observed major-axis component of velocity at P31 or P32, the subscript "2" indicates similarly directed components at locations where velocities computed from model and directly measured in the field are both available, "obs" stands for "observed," and "comp" stands for "computed."

According to (42), prediction by persistance ($v_{2_{comp}} = v'_{1_{obs}}$) scores zero, and a large negative score result in cases where the alongshore variation is small and not well-predicted. Table 2 presents a summary of mdoel skill computations for three pairs of stations, (P31, P11), (P31, 36) and (P32, P12). There are substantial amount of skill in all cases. The skill is particularly high in the prediction of observed alongshore variations, between Stations P31 and 36, in major-axis velocity fluctuations. The absolute error defined as a normalized standard deviation (Hsueh and Lee, 1978) in the predicted velocity field, ranges from 9% at Station P12 to 52% at Station 36 and is reasonably low. As the velocity time series at Stations P31 and P32 are quite similar, the result of the skill computation is probably not very sensitive as to whether P31 or P32 are used as the upstream station. In any event, with flows on the Long Island shelf monitored, the chance is quite good that the time-dependent flows in the HSV and on the New Jersey shelf may be predicted with a simple wind-driven model such as the one developed here.

Table 2

Summary of skills and statistics for velocity components along local major axes

Station	Variance		Skill	Abs Error
	10^3 cm^2/sec^2		%	%
	OBS	Model		
P11	9.31	20.5	57	32
P12	21.1	21.3	20	9
36	28.3	15.1	82	53

5. Discussion

The success of the composite, New York Bight circulation model, although considerable, is nevertheless clearly limited in a number of ways. The difficulty encountered in predicting minor-axis velocities is common to all continental shelf circulation models that deals with a cut-away section of the continental shelf (Hsueh, 1980). Aside from the fact that the backward boundary condition transmits no upstream information in cross-shelf velocities, the forced response to winds that are included in the model is largely confined to a parabolic coastal boundary layer, emanating from the point where the backward boundary meets the coast, and is not expected to assert itself shelf-wide until a certain distance upstream is reached (Csanady, 1978). This distance is given by $sL^2/4\delta$ where s stands for the slope of the continental shelf. Over the New York Bight, this distance is approximately 250 km, nearly the entire length of the model coverage. Thus, on the whole, comparisons of minor-axis velocity components between model results and the observation is better in the HSV and on the New Jersey shelf than over the Long Island shelf. Fig. 15 presents a contrast between two such comparisions. At Station 30, the model response is weak, while at Station 36, 33 km up the coast and 17 km inshore, the model response is substantial and bears some resemblance to the observed in fluctuations.

The construction of the composite model also requires matching the CSW models for the Long Island and New Jersey shelves to the RTW model for the HSV. The governing equations for pressure for both the CSW and RTW models are approximations to the following complete equation:

$$H \nabla^2 p_t + \nabla H \cdot \nabla p_t - fJ(p,H) + f\delta\nabla^2 p = 0. \qquad (43)$$

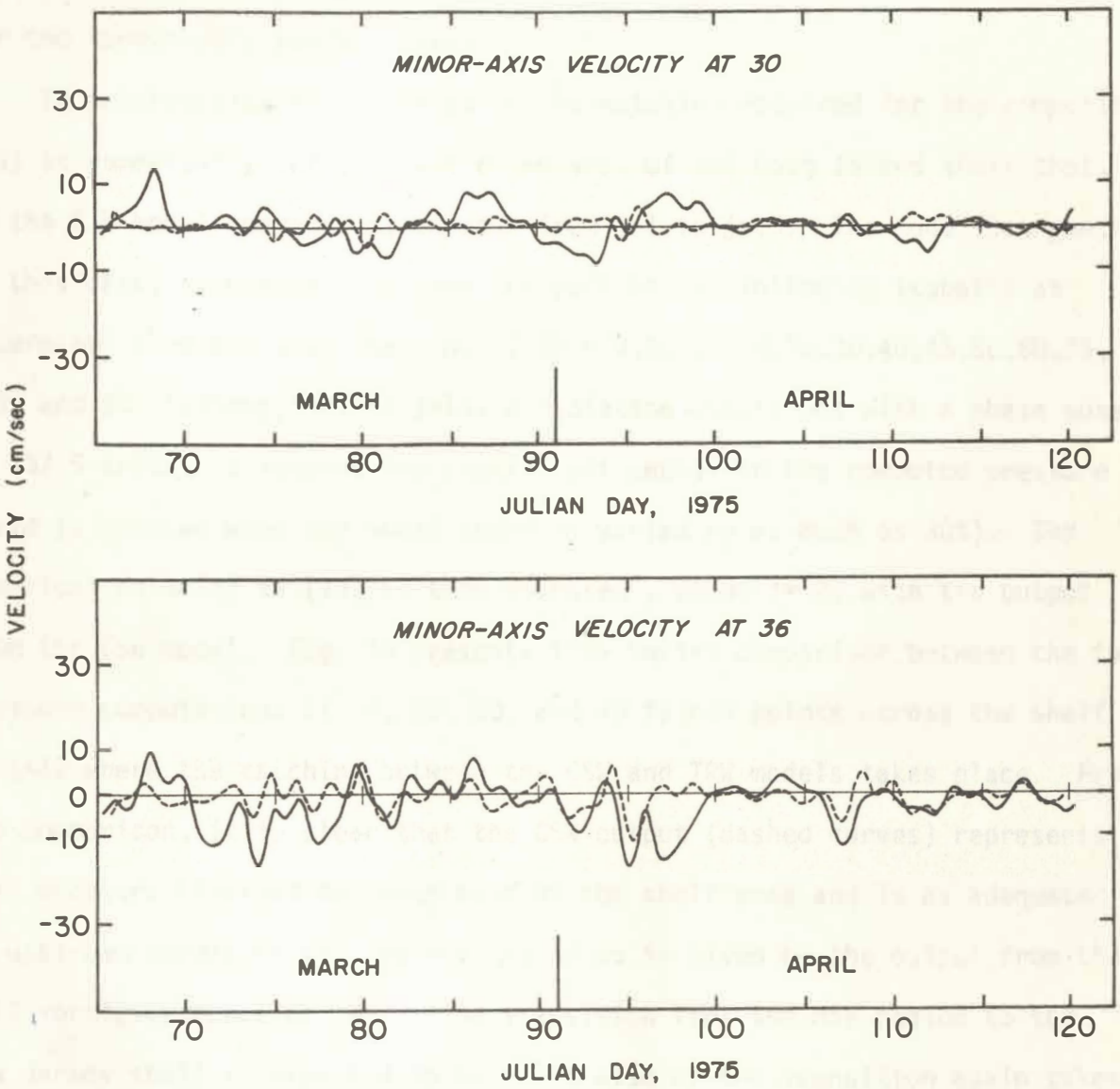

Fig. 15. Time series comparison of minor-axis velocities at (a) mooring station 30 and (b) mooring station 36. The solid curves represent the 40-hour low-pass-filtered observations along the observed minor axes and the dashed curves represents model results along model minor axes. See Fig. 6 for the major axis orientations. The minor axis is perpendicular to the major axis.

In the long wave limit, (43) reduces to (5) in its homogeneous form. In the limit of quasi-geostrophy, (43) reduces to (6) (with zero wind-stress curl) for the topographic Rossby waves.

To substantiate the validity of the matching required for the composite, (43) is numerically integrated over an area of the Long Island shelf that, in the CSW model convention, extends from j=1 to j=15. The model bathymetry, in this case, is constructed from the path of the following isobaths as determined from the CG&S chart No. 1108 = 0,10,15,20,25,30,40,45,50,60,75, 100, and 500 fathoms. Along j=15, a radiation conditions with a phase speed of 937.5 km/day is imposed (no significant change in the computed pressure field is noticed when the phase speed is varied by as much as 30%). The numerical solution to (43) is then compared , along j=12, with the output from the CSW model. Fig. 16 presents time series comparison between the two pressure computations at 10, 20, 30, and 40 fathom points across the shelf at j=12 where the matching between the CSW and TRW models takes place. From the comparison, it is clear that the CSW output (dashed curves) represents well pressure fluctuations over most of the shelf area and is as adequate an upstream condition for the HSV region as is given by the output from the full vorticity equation (43). The transition from the HSV region to the New Jersey shelf is expected to be valid also as the transition again takes place in a stretch of the shelf where the bathymetry is turning smooth (see Fig. 1). Since the CSW model is much more economic to run, the fact that it is also adequate for most of the shelf area represents a substantial saving in computing resources.

In contrast to the Long Island and New Jersey shelves for which relatively simple computational scheme appears to work adequately, the HSV

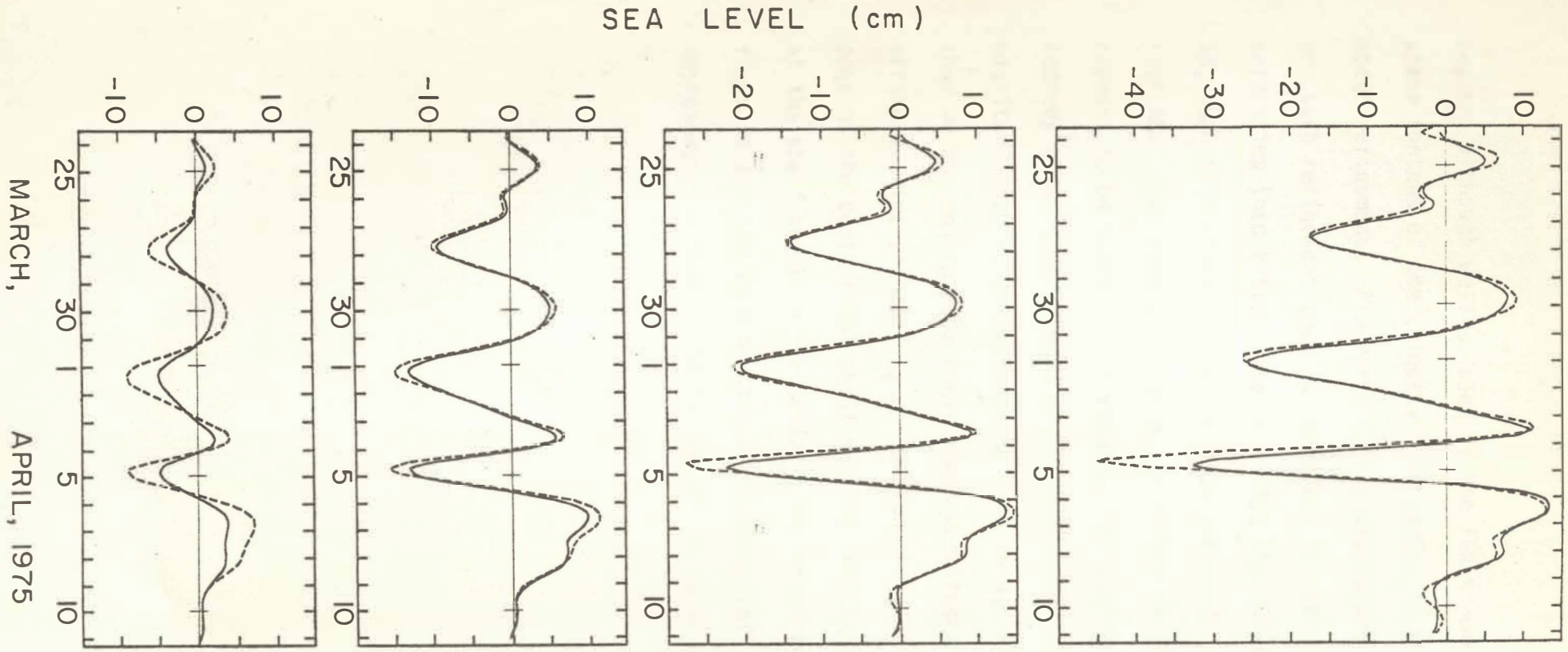

Fig. 16. Time series comparisons between pressure fluctuations computed from the long-wave approximation to the barotropic vorticity equation and those computed from the full barotropic voriticity equation. The comparisons are made at locations with local depth of (a) 10-fathom, (b) 20-fathom, (c) 30-fathom, and (d) 40-fathom along the cross-shelf transect between the Long Island shelf region and the Hudson Shelf Valley region. The time period for which the comparisons are made is 24 March - 11 April, 1975. The solid curve represents pressure fluctuations computed from the long wave approximation and the dashed curve represents those computed from the full equation model. The latter extends further offshore to the 500-fathom isobath. This accounts for the large amplitude difference at the 40-fathom location.

region, although well-modeled by the TRW scheme in the sense that the observed phase content of the velocity time series is reproduced, clearly awaits further model refinement. Finer resolution alongshore than that used appears to be one such refinement that is necessary for bringing the amplitude of the model velocities into better agreement with the observation, especially at Station 33, than that which has so for been achieved. A shaprer model valley formation than that used also makes for a more realistic long wave reflection that appears to be operative in nature. The use of winds observed at the John F. Kennedy airport is suspect also. Over-water winds are generally greater in magnitude than winds measured on land (Hsu, 1981). Over-land winds must thus be compensated for their small magnitudes before they become applicable offshore. The possibility of an alongshore pressure gradient on the seaward edge of the continental shelf must be admitted. The non-adiabetic forcing at the shelf break is particularly important during periods of southwestward flows in the New York Bight. Until these refinements are made, no substantive improvement in model calculation can be expected.

6. Conclusion

A composite, numerical model of the winter-time circulation of New York Bight is developed. The long wave limit is taken on the Long Island and New Jersey shelves of the barotropic vorticity balance that is believed to represent the primary dynamics on the continental margin. In the Hudson Shelf Valley region where the bathymetry undergoes abrupt change alongshore, a quasi-geostrophic approximation is thought to apply instead. The cross-shelf distribution in pressure is matched between the HSV region and the two shelves. The model is forced by surface winds observed at the John F. Kennedy airport and by cross-shelf pressure distribution derived from alongshore currents observed along a transect near Shinnecock, New York. The numerical results, for the period of 7 March-30 April 1975, in terms of velocities along local major axes are compared to directly measured currents at Stations 29 and 30 on the Long Island shelf, at Stations 33 and 36 in the HSV, and at Stations 49, P11 and P12 on the New Jersey shelf. There is good agreement at all stations. A significant amount of model skill is also found in the prediction of alongshore difference between input stations, along which a "backward" boundary condition is imposed, and a number of interior stations.

Upon reaching the HSV, the flow is guided by bathymetry and bottom friction to go along the valley axis. The net result is an upvalley flow in response to wind-driven shelf flows to the northeast and a downvalley flow in response to backward-boundary-condition-driven flows to the southwest. The vorticity balance that is involved in the channeling of the flow during an individual event is essentially that of a steady-state flow. Consequently, steady-state results remain valid as an event-average of the time-dependent flow in the HSV.

Discrepancies between model results and the observation point to the need of incorporating into the model an alongshore pressure gradient on the offshore boundary of the shelf and the need to resolve better the formation of the HSV. These are, however, refinements that are easily instilled. As is, the composite model remains a success and should prove useful in further studies of the circulation in the New York Bight.

References

Beardsley, Robert C. and William C. Boicourt, 1981: On estuarine and continental-shelf circulation in the Middle Atlantic Bight. In Evolution of Physical Oceanography. Edited by B.A. Warren and Carl Wunsch. MIT Pres., Cambridge, Massachusetts, 623 pp.

Brink, K.H., 1982: Low frequency free wave and wind-driven motions over a submarine bank. Manuscript.

Csanady, G.T., 1978: The arrested topographic wave. J. Phys. Oceanogr., 8, 47-72.

Hsu, S.A., 1981: Models for estimating offshore winds from onshore meteorological measurements. Bound-Layer Meteor., 20, 341-351.

Hsueh, Y. and Chi-Yuan Lee, 1978: A hindcast of barotropic response over the Oregon-Washington continental shelf during the summer of 1972. J. Phys. Oceanogr., 8, 799-810.

Hsueh, Y., 1980: On the theory of deep flow in the Hudson Shelf Valley. J. Geophys. Res., 85, 4913-4918.

Kundu, P.K., 1976: Ekman veering observed near the ocean bottom. J. Phys. Oceanogr., 6, 238-242.

Mayer, Dennis A., Donald V. Hansen, and Donald A. Ortman, 1979: Long-term current and temperature observations on the Middle Atlantic Shelf. J. Geophys. Res., 84, 1776-1791.

Acknowledgements

The authors acknowledge the generosity of D.V. Hansen and G. Han in supplying all the necessary data for this study. The research is supported by the National Oceanic and Atmospheric Administration grant 04-6-022-44026 and a supplement thereof through P.O. #NA-81-RCA-580.